

1 **Differences in aerosol and cloud properties along the central**
2 **California coast when winds change from northerly to southerly**

3
4 Kira Zeider¹, Grace Betito², Anthony Bucholtz³, Peng Xian⁴, Annette Walker⁴, Armin
5 Sorooshian^{1,2*}

6
7 ¹Department of Chemical and Environmental Engineering, University of Arizona, Tucson, Arizona, 85721, USA

8 ²Department of Hydrology and Atmospheric Sciences, University of Arizona, Tucson, Arizona, 85721, USA

9 ³Department of Meteorology, Naval Postgraduate School, Monterey, California, 93943, USA

10 ⁴Marine Meteorology Division, Naval Research Laboratory, Monterey, California, 93943, USA

11
12
13 **Correspondence to:* Armin Sorooshian (armin@arizona.edu)

16 **Abstract.** Wind reversals resulting in southerly flow along the California coast are not well understood in terms of
17 how aerosol and cloud characteristics change. This gap is addressed using airborne field measurements enhanced with
18 data from space-borne remote sensing (Moderate Resolution Imaging Spectroradiometer), surface stations
19 (Interagency Monitoring of Protected Visual Environments), and models (Navy Aerosol Analysis and Prediction
20 System and Coupled Ocean/Atmosphere Mesoscale Prediction System), with a focus on sub- and supermicron aerosol,
21 and cloud microphysical variables: cloud droplet number concentration (N_d), cloud optical thickness (COT), and cloud
22 droplet effective radius (r_e). Southerly flow coincided with higher values of submicron aerosol concentration (N_a) and
23 mass concentrations of species representative of fine aerosol pollution (NO_3^- and nss-SO_4^{2-}) and shipping/continental
24 emissions (V, oxalate, NH_4^+ , Ni, OC, and EC). Supermicron N_a did not change, however, heightened levels of acidic
25 species in southerly flow coincided with reduced $\text{Cl}^-:\text{Na}^+$ suggestive of Cl^- depletion in salt particles. Clouds responded
26 correspondingly in southerly flow, with more acidic cloud water, higher levels of similar species as in the aerosol
27 phase (e.g., NO_3^- , nss-SO_4^{2-} , NH_4^+ , V), along with elevated values of N_d and COT and reduced r_e during campaigns
28 with similar cloud liquid water paths. Case study flights help to visualize offshore pollution gradients and highlight
29 the sensitivity of the results to the presence of widespread smoke coverage including how associated plumes have
30 enhanced supermicron N_a . These results have implications for aerosol-cloud interactions during wind reversals, and
31 have relevance for weather, public welfare, and aviation.

1 Introduction

The northeastern Pacific Ocean is one of the most heavily studied regions as it relates to aerosol-cloud interactions due to the persistent and spatially broad stratocumulus cloud deck that is influenced by a variety of emissions sources, notably shipping (Wood, 2012; Russell et al., 2013). One aspect of that region that warrants more attention is the predominant direction of lower tropospheric winds, as recent work has suggested that it can have significant implications for aerosol and cloud properties (Juliano et al., 2019a; 2019b; [Juliano and Lebo, 2020](#)). The wind direction along the North American west coast is influenced by its topography, namely the coastal mountains (e.g., National Research Council, 1992), and during the California (CA) warm season (April through September) it is primarily from the north along the coast. An important weather phenomenon during that season is the infrequent and short-lived (from one to several days) transition from northerly to southerly flow near the coast up to 100 km offshore (e.g., Nuss et al., 2000). Particularly, the northerly winds weaken (e.g., Winant et al., 1987; Melton et al., 2009) and eventually reverse. Along with a decrease in temperature and increases in pressure and cloud fraction (e.g., increases in low clouds and fog), there is also a change in overall wind speed: most northerlies (~75%) have a wind speed component less than 5 m s^{-1} (Bond et al., 1996), whereas southerly “surges” are characterized by sudden increases in wind speed to 15 m s^{-1} or greater (Mass and Albright, 1987). This is not a phenomenon that is unique to the U.S.; a handful of studies have noted these events along the coasts of South America (e.g., Garreaud et al., 2002; Garreaud and Rutllant, 2003), southern Africa (e.g., Reason and Jury, 1990), and even Australia (e.g., Holland and Leslie, 1986; Reason et al., 1999; Reid and Leslie, 1999).

These wind reversals – referred to as either coastally trapped disturbances (CTDs), coastally trapped wind reversals (CTWRs), stratus surges, or southerly surges, to name a few – have been studied since the 1970s (Gill, 1977; Dorman, 1985). There have been a fair number of publications discussing the dynamics and forcing mechanisms for such events (thoroughly reviewed by Nuss et al., 2000) primarily using data from buoys, radars, and research aircraft. Buoy (e.g., Bond et al., 1996) and satellite studies (e.g., Parish, 2000; Rahn and Parish, 2010) mainly discussed the topics related to mesoscale structure, while the research aircraft studies (e.g., Ralph et al., 1998; Rahn and Parish, 2007) have attempted to document physical characteristics of the wind reversal. For example, Rahn and Parish (2007) used sawtooth maneuvers to depict the vertical structure of the 22-25 June 2006 reversal through examining surface pressure, temperature, wind direction, wind speed, along-shore wind, and cross-shore wind. Additionally, there have been multiple studies attempting to model these wind reversals (e.g., Rogerson and Samelson, 1995; Guan et al., 1998; Skamarock et al., 1999; Mass and Steenburgh, 2000; Thompson et al., 2005) to better understand their initiation, propagation, and cessation. These studies found that CTDs are initiated by changes in synoptic-scale flow, particularly offshore, and that the coastal mountains dampen the flow, deepen the marine layer, and propagate a mesoscale coastal ridge of higher pressure northward that ultimately leads to the development of a coastally trapped southerly wind component.

However, there have been limited attempts to look into aerosol and cloud characteristics during a southerly surge (e.g., Juliano et al., 2019a; 2019b), and among them were studies that happened to encounter them by chance without these surges having been the study’s focus (Crosbie et al., 2016; Dadashazar et al., 2020). Juliano et al. (2019a) was, to our best knowledge, the first study to focus on CTD aerosol-cloud interactions using 23 cases identified between 2004 and 2016 with buoy data and satellite imagery. They found notable differing characteristics between non-CTD (northerly flow) and CTD (southerly flow) conditions, with higher cloud droplet number concentration (N_d) and lower droplet effective radius (r_e) for CTD cases. Compared to non-CTD events, CTD events had r_e values that were ~20-40% lower (i.e., differences often exceeding $\sim 3 \mu\text{m}$) and N_d values ($\sim 250 \text{ cm}^{-3}$) that were almost twice as large in many areas. They attributed this to some combination of (i) mixing of sea salt particles into the boundary layer due to an observed wind stress-sea surface temperature cycle; (ii) offshore flow transporting continental aerosol into areas offshore of CA; and (iii) extended periods of time that southerly air spends in shipping lanes. Some continental sources they noted include agricultural emissions from the CA Central Valley, biogenic emissions from various major sources such as forests around Oregon and northern CA, smoke from biomass burning, and urban emissions from major CA cities such as Los Angeles, San Jose, Sacramento, and San Francisco. These sources have been confirmed in various studies conducted in coastal areas of central CA (Wang et al., 2014; Maudlin et al., 2015; Braun et al., 2017; Dadashazar et al., 2019; Ma et al., 2019). A subsequent study (Juliano et al., 2019b) analyzed three CTD events using satellite and aircraft observations, as well as numerical simulations. That study’s usage of aircraft data was limited to cloud water composition, to support results from their previous study that non-CTD days were primarily influenced by marine sources like sea salt, whereas CTD days exhibited more relative influence from continental and shipping

84 (i.e., higher SO_4^{2-} and NO_3^-) sources. Those studies noted that additional observations, specifically of an in situ nature,
85 were needed to confirm results that were mostly based on modeling and remote sensing.

86 The goal of this study is to contrast aerosol and cloud characteristics between southerly and northerly flow
87 regimes in the lower troposphere (below 3 km) offshore of central CA. Note that ~~we do not focus here on this study's~~
88 ~~primary objective is not to characterize~~ meteorological and large-scale features associated with wind reversals and ~~we~~
89 do not classify events based on whether they are CTDs but ~~focus exclusively rather categorize events based on~~
90 boundary layer wind direction. As a way to address the shortage of in situ observational data used for this research
91 application, an important inventory of airborne data ~~are~~is leveraged that have been collected over the last two decades
92 (Sorooshian et al., 2018) that afford increased ~~statistics~~sampling density of southerly flow cases relative to Juliano et
93 al. (2019b). Such cases are difficult to sample owing to their lower frequencies (Table 1) compared to days with
94 northerly flow and because aircraft flights do not occur each day, so some southerly cases are missed during airborne
95 campaigns. In total, 17 days of data exist from Naval Postgraduate School (NPS) Twin Otter campaigns coinciding
96 with southerly flow, with some days including multiple flights. One thing that has yet to happen in past studies is to
97 use in situ data to compare more than just cloud water composition but also relevant variables such as aerosol number
98 concentration (N_a) and N_d , which is crucial to intercompare with satellite data and put previous speculations about
99 aerosol and cloud responses to southerly flow on sturdier ground. As the aircraft data are still limited, we complement
100 the analysis with other datasets, including those from satellite remote sensors, models, and surface stations.

101 The structure of this paper is as follows: Sect. 2 reports on methods used; Sect. 3 shows results beginning
102 with a discussion of how well a model can represent southerly winds, followed by assessing how well the datasets
103 show more fine pollution during southerly days and if clouds respond accordingly with the usual chain of events
104 associated with the Twomey effect (Twomey, 1974) whereby clouds have more but smaller drops at similar liquid
105 water path; and Sect. 4 provides conclusions. The results of this work have implications for numerous societal and
106 environmental factors sensitive to aerosol and cloud characteristics such as transportation (especially aviation),
107 agriculture, biogeochemical cycling of nutrients and contaminants, and coastal ecology (Dadashazar et al., 2020).

108 2 Methods

109 This study relies on the use of multiple datasets to examine how aerosol and cloud characteristics vary
110 between traditional northerly flow along the CA coastline as compared to less common southerly flow periods. This
111 study was initially inspired by airborne field measurements (Table 1) whereby on a few opportune flight days,
112 southerly flow was encountered off the CA coast. Because these events were rare in comparison to the majority of
113 flights with northerly flow (Southerly Winds % in Table 1), several campaigns worth of data are compiled to ~~build~~
114 ~~more statistics of~~increase data points for southerly flow days. The airborne data used here are all from summer periods,
115 which is when most field studies have focused on this region to investigate aerosol-cloud interactions (e.g., Russell et
116 al., 2013) allowing for easier intercomparison for interested readers. We enhance ~~statistics~~data volume by also
117 conducting complementary analyses with data obtained from ~~space-borne~~spaceborne remote sensing, surface-based
118 stations, and models. Below we first describe the airborne datasets, followed by the wind classification method, and
119 then descriptions of the models, surface data, and satellite data.

120 2.1 Airborne Field Missions

121 This study utilizes data from six airborne missions based out of Marina, CA (~~white diamond~~; Fig. 1) using
122 the Naval Postgraduate School (NPS) Twin Otter aircraft. ~~Marina is approximately 5 km away from the coastline~~. The
123 scientific target of these campaigns included a mix of aerosol-cloud interactions, aerosol microphysical processes, and
124 characterization of wildfire emissions: the Eastern Pacific Emitted Aerosol Cloud Experiment (E-PEACE), the
125 Nucleation in California Experiment (NiCE), the Biological and Oceanic Atmospheric Study (BOAS), the Fog and
126 Stratocumulus Evolution Experiment (FASE), the Marine Aerosol Cloud And Wildfire Study (MACAWS), and the
127 California Smoke Mission (CSM) (Table 1). Another Twin Otter mission from 2019 (Monterey Aerosol Research
128 Campaign - MONARC) is not included in this analysis due to the lack of southerly flow days sampled during the
129 campaign. The research flight (RF) paths for each campaign are shown in Fig. 1. In some instances, multiple flights
130 were conducted on a single day, either to capture time-sensitive atmospheric features or to collect data beyond the
131 endurance limit of the instrumented aircraft. For those days, RFs are assigned the same number but are distinguished
132 with endings 'A,' 'B,' and 'C,' for successive flights, respectively. E-PEACE and NiCE had the most cases of
133 southerly flow owing partly to those campaigns having had the most flights: five out of 30 flights for E-PEACE; four
134
135

136 out of 23 flights for NiCE. BOAS also had four flights with southerly flow (out of 15 flights)) but they were spread
 137 across two flights days as compared to E-PEACE and NiCE whose southerly flights were all on distinct days.

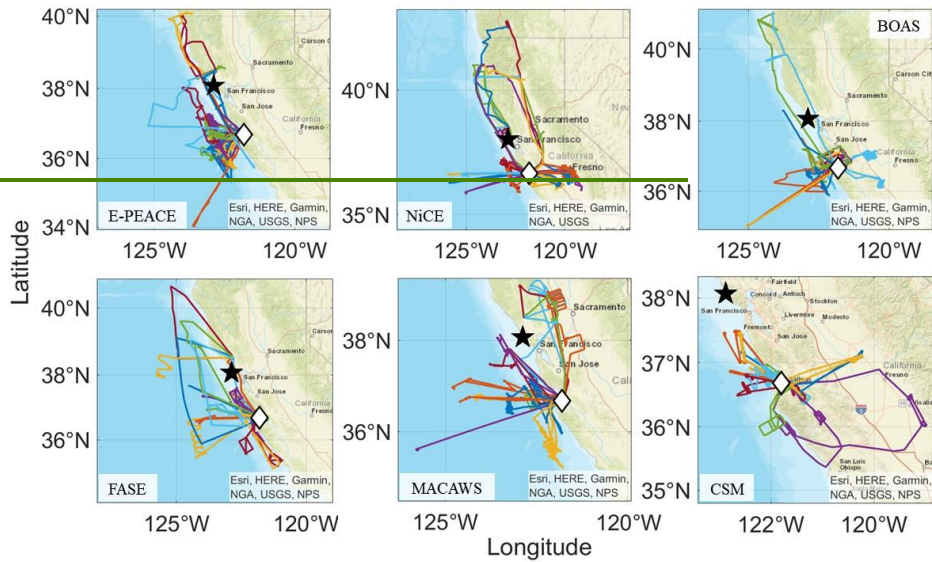
138 The Twin Otter flew at $\sim 55 \text{ m s}^{-1}$ and conducted measurements during level legs and sounding profiles, over
 139 both the land and the ocean, and within and above the boundary layer during flight periods ranging from one to five
 140 hours. Additional information regarding aircraft and flight characteristics, as well as the general flight strategy is
 141 summarized in Sorooshian et al. (2019). The general area of focus in this study was within the following range of
 142 coordinates, with many of the results specifically targeting just the ocean areas in this spatial domain: $35.31^\circ \text{ N} -$
 143 40.99° N , $125.93^\circ \text{ W} - 118.98^\circ \text{ W}$.

144 This study's analysis focuses on maximizing the number of southerly and northerly cases available from the
 145 flight data rather than keeping a similar number of flights to represent southerly and northerly conditions. The rationale
 146 to include all available northerly flight days (which exceed southerly days; Table 1) is that their combined use is more
 147 representative of typical northerly conditions and less sensitive to inter-day variations. That being said, a random
 148 selection of northerly flight days was still used to compare to the more limited number of southerly flight days (not
 149 shown here), with the same general conclusions reached as compared to using all northerly flight days.

150
 151 **Table 1: Summary of NPS Twin Otter campaigns used in this study, including dates, number of RFs per campaign, RFs**
 152 **that are categorized as having had southerly flow, and percentage of southerly days during the campaign period (including**
 153 **all days in those months and not just RF days). Days are categorized as having southerly flow based on the analysis in Sect.**
 154 **2.2.**

Campaign	Dates	Total RFs	RF # (Flight Date) with Southerly Winds	Southerly Winds % (# Southerly days / Total days in period)
E-PEACE	07/08 – 08/18/2011	30	RF11 (07/23), RF12 (07/24), RF14 (07/27), RF15 (07/28), RF16 (07/29)	12.90% (8/62)
NiCE	07/08 – 08/07/2013	23	RF7 (07/16), RF8 (07/17), RF9 (07/18), RF16 (07/29)	14.52% (9/62)
BOAS	07/02 – 07/24/2015	15	RF10A & 10B (07/16), RF11A & 11B (07/17)	32.26% (10/31)
FASE	07/18 – 08/12/2016	16	RF6A, 6B, & 6C (07/29)	14.52% (9/62)
MACAWS	06/21 – 07/12/2018	16	RF12 (07/05), RF16 (07/12)	4.92% (3/61)
CSM	09/01 – 09/25/2020	14	RF1 (09/01), RF5 (09/09), RF6 (09/10)	13.33% (4/30)

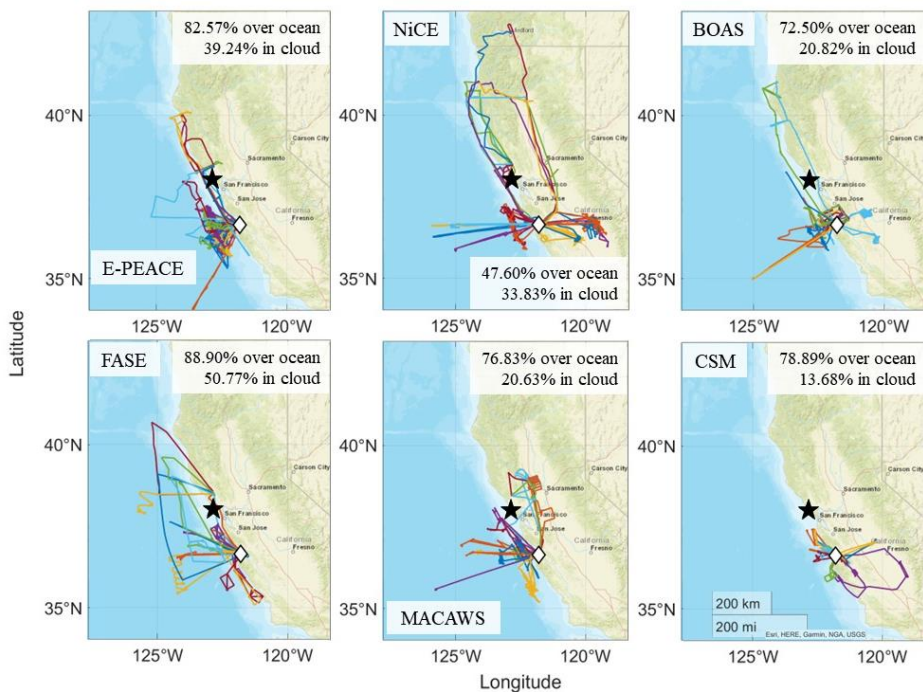
155
 156



157

<u>Campaign</u>	<u>Dates</u>	<u>Total RFs</u>	<u>RF # (Flight Date) with Southerly Winds</u>	<u>Southerly Winds % (# Southerly days / Total days in period)</u>
<u>E-PEACE</u>	<u>07/08 – 08/18/2011</u>	<u>30</u>	<u>RF11 (07/23), RF12 (07/24), RF14 (07/27), RF15 (07/28), RF16 (07/29)</u>	<u>12.90% (8/62)</u>
<u>NiCE</u>	<u>07/08 – 08/07/2013</u>	<u>23</u>	<u>RF7 (07/16), RF8 (07/17), RF9 (07/18), RF16 (07/29)</u>	<u>14.52% (9/62)</u>
<u>BOAS</u>	<u>07/02 – 07/24/2015</u>	<u>15</u>	<u>RF10A & 10B (07/16), RF11A & 11B (07/17)</u>	<u>32.26% (10/31)</u>
<u>FASE</u>	<u>07/18 – 08/12/2016</u>	<u>16</u>	<u>RF6A, 6B, & 6C (07/29)</u>	<u>14.52% (9/62)</u>
<u>MACAWS</u>	<u>06/21 – 07/12/2018</u>	<u>16</u>	<u>RF12 (07/05), RF16 (07/12)</u>	<u>4.92% (3/61)</u>
<u>CSM</u>	<u>09/01 – 09/25/2020</u>	<u>14</u>	<u>RF1 (09/01), RF5 (09/09), RF6 (09/10)</u>	<u>13.33% (4/30)</u>

158



159
 160 **Figure 1: Research flight paths for the six Twin Otter campaigns used in this study. The aircraft base at Marina, CA is**
 161 **denoted by a white diamond, and the IMPROVE station used in this study is indicated by a black star (Pt. Reyes National**
 162 **Seashore). The legends in each panel report on the percentage of flight time spent over the ocean and in cloud over the**
 163 **ocean.**
 164

165 **2.1.1 Twin Otter Instrumentation**

166 Table 2 summarizes the relevant instruments used for each Twin Otter mission pertinent to this work. More
 167 extensive details about the instruments, and those not listed below such as relevant navigational and meteorological
 168 instruments, are described in Sorooshian et al. (2018).
 169

170 **Table 2: Summary of Twin Otter payload during the field campaigns used for this study. The six farthest right columns**
 171 **show instrument availability for each campaign.**

Instrument	Measured variable	Size range	Time resolution	E-PEACE	NiCE	BOAS	FASE	MACAWS	CSM
TSI Ultra-fine Condensation Particle Counter (CPC) 3025	$N_{a>3nm}$	> 0.003 μm	1 s	X	X	X	X	X	X
TSI Condensation Particle Counter (CPC) 3010	$N_{a>10nm}$	> 0.01 μm	1 s	X	X	X	X	X	X
PMS/DMT Passive Cavity Aerosol Spectrometer Probe (PCASP)	$N_{a0.1-1\mu m}$ $N_{a>1\mu m}$	~0.1 – 3.4 μm	1 s	X	X	X	X	X	X
DMT Cloud and Aerosol Spectrometer - Forward Scattering (CASF)	N_d	~0.6 - 60 μm	1 s	X	X		X	X	X
PMS/DMT Forward Scattering Spectrometer Probe (FSSP)	N_d	1 - 46 μm	1 s		X	X	X	X	
ARI Aerosol Mass Spectrometer (AMS)	Speciated mass conc.	~60 - 600 nm	< 15 s	X	X	X			
Mohnen Cloud Water Collector - pH, IC, ICPMS	pH, air-equivalent mass conc.	N/A	~ 5 - 60 min	X	X	X	X	X	

172

Instrument	Measured variable	Size range	Time resolution	E-PEACE	NiCE	BOAS	FASE	MACAWS	CSM
<u>TSI Ultra-fine Condensation Particle Counter (CPC) 3025</u>	<u>$N_{a>3nm}$</u>	<u>> 0.003 μm</u>	<u>1 s</u>	<u>X</u>	<u>X</u>	<u>X</u>	<u>X</u>	<u>X</u>	<u>X</u>
<u>TSI Condensation Particle Counter (CPC) 3010</u>	<u>$N_{a>10nm}$</u>	<u>> 0.01 μm</u>	<u>1 s</u>	<u>X</u>	<u>X</u>	<u>X</u>	<u>X</u>	<u>X</u>	<u>X</u>
<u>PMS/DMT Passive Cavity Aerosol Spectrometer Probe (PCASP)</u>	<u>$N_{a0.1-1\mu m}$ $N_{a>1\mu m}$</u>	<u>~0.1 – 3.4 μm</u>	<u>1 s</u>	<u>X</u>	<u>X</u>	<u>X</u>	<u>X</u>	<u>X</u>	<u>X</u>
<u>DMT Cloud and Aerosol Spectrometer - Forward Scattering (CASF)</u>	<u>N_d</u>	<u>~0.6 - 60 μm</u>	<u>1 s</u>	<u>X</u>	<u>X</u>		<u>X</u>	<u>X</u>	<u>X</u>
<u>PMS/DMT Forward Scattering Spectrometer Probe (FSSP)</u>	<u>N_d</u>	<u>1 - 46 μm</u>	<u>1 s</u>		<u>X</u>	<u>X</u>	<u>X</u>	<u>X</u>	
<u>ARI Aerosol Mass Spectrometer (AMS)</u>	<u>Speciated mass conc.</u>	<u>~60 - 600 nm</u>	<u>< 15 s</u>	<u>X</u>	<u>X</u>	<u>X</u>			
<u>Mohnen Cloud Water Collector - pH, IC, ICPMS</u>	<u>pH, air-equivalent mass conc.</u>	<u>N/A</u>	<u>~ 5 - 60 min</u>	<u>X</u>	<u>X</u>	<u>X</u>	<u>X</u>	<u>X</u>	

173

174 Condensation particle counters (CPCs; TSI, Inc.) were used to measure particle number concentrations for
 175 diameters greater than 3 (N_{a>3nm} or N_{a3}) and 10 nm (N_{a>10nm} or N_{a10}), respectively, as well as the Passive Cavity Aerosol
 176 Spectrometer Probe (PCASP; Particle Measuring Systems (PMS), Inc., modified by Droplet Measurement
 177 Technologies (DMT), Inc.) for diameters between ~100 nm and 3.4 μm. The Cloud and Aerosol Spectrometer –
 178 Forward Scattering (CASF; DMT, Inc.) measured the size distribution of larger particles and droplets between 0.6 –
 179 60 μm for all missions except for BOAS when the Forward Scattering Spectrometer Probe (FSSP; PMS, Inc. modified
 180 by DMT, Inc.) was used in its place. The cloud probes were calibrated before each field campaign to ensure
 181 consistency between the instruments (Sorooshian et al., 2018). The CASF and FSSP size distributions were integrated
 182 to determine total N_a and liquid water content (LWC) when the aircraft was in cloud using the criterion of LWC
 183 ~~needing to exceed~~ $\geq 0.02 \text{ g m}^{-3}$; all instances of LWC ~~less than~~ $< 0.02 \text{ g m}^{-3}$ were considered cloud-free and only
 184 considered for quantification of aerosol variables such as total N_a in different size ranges (Fig. S1). Additionally, RFs
 185 categorized as southerly flow were filtered to only include data during periods when the horizontal wind direction was
 186 between 135° and 225°. A variety of statistics were calculated for the reported and derived variables (e.g., N_{a>3nm},
 187 N_{a>10nm}, N_{a10-100nm} (N_{a>10nm} - N_{a0.1-1μm}), N_{a0.1-1μm}, N_{a>1μm}, the ratio of N_{a3} to N_{a10} (N_{a3}:N_{a10}), N_a, horizontal wind speed
 188 and direction) in categories of interest including medians and minimum/maximum values. The mode ~~wind direction~~
 189 was calculated ~~for wind direction~~ for each RF as well as each overall campaign, since that statistic is assumed here to
 190 be a better representation of typical wind directions rather than the median.

191 An Aerosol Mass Spectrometer (AMS; Aerodyne Research Inc. (ARI)) was used during some campaigns to
 192 measure sub-micrometer (submicron) aerosol composition, specifically for non-refractory components (SO₄²⁻, NO₃⁻,
 193 NH₄⁺, Cl⁻, and organics). Coggon et al. (2012; 2014) discuss in detail the AMS operational details and results from
 194 some of the campaigns. Cloud water (CW) was collected using a Mohnen CW collector, which was manually placed
 195 above the fuselage of the Twin Otter during cloud penetrations for sample collection into vials kept inside the aircraft.
 196 After flights, samples were analyzed for pH and speciated concentrations of various water-soluble ions and elements,
 197 with a number of studies summarizing the operational details and selected results (e.g., Wang et al., 2014; Wang et
 198 al., 2016; ~~MaedonaldMacDonald~~ et al., 2018). An Oakton Model 110 pH meter was used for E-PEACE, NiCE, and
 199 BOAS, and a Thermo Scientific Orion 8103BNUWP Ross Ultra Semi-Micro pH probe was used for FASE and
 200 MACAWS. Water-soluble ionic composition was measured via Ion Chromatography (IC; Thermo Scientific Dionex
 201 ICS – 2100 system), except some ions during E-PEACE, including Na⁺, could not be measured. Water-soluble
 202 elemental composition was measured via Inductively Coupled Plasma Mass Spectrometry (ICP-MS; Agilent 7700
 203 Series) for E-PEACE, NiCE, and BOAS, and via Triple Quadrupole Inductively Coupled Plasma Mass Spectrometry
 204 (ICP-QQQ; Agilent 8800 Series) for FASE and MACAWS. Cloud water was not collected during CSM. The IC
 205 species analyzed in this study are Cl⁻, NH₄⁺, NO₃⁻, non-sea salt (nss)-SO₄²⁻, and oxalate, and the ICPMS species
 206 analyzed are Ca²⁺, K⁺, Na⁺, and V. We used the following equation to calculate nss-SO₄²⁻ under the assumption that
 207 all Na⁺ is from sea salt (e.g., AzadiAghdam et al., 2019):

$$209 \quad [nss - SO_4^{2-}] = [SO_4^{2-}] - 0.253 \times [Na^+] \quad (1)$$

210
 211 Aqueous concentrations of ions and elements were converted into air-equivalent concentrations using the mean LWC
 212 encountered when the aircraft was in cloud (LWC > 0.02 g m⁻³) during collection of individual samples.

213 Aircraft data were analyzed four different ways over the study domain. The primary focus of the analysis is
 214 using data within the spatial domain listed in Sect. 2.1 only when the aircraft was over the ocean- (Fig 1). In addition
 215 to a LWC maximum of 0.02 g m⁻³, another screening criterion was utilized to omit data during RFs strongly influenced
 216 by wildfire emissions (Table 3), which was when the median flight-wide N_{a>10nm} value exceeded 7,000 cm⁻³ for
 217 altitudes less than 800 m. This value was determined by closely examining flights that flew through areas with reported
 218 wildfire influence using flight notes. Data were alternatively analyzed for RF segments only over the ocean without
 219 the N_{a>10nm} criterion applied, and then also when the aircraft flew within the spatial domain over land and ocean both
 220 with and without the same wildfire criterion; those results are shown in Tables S1 - S3. Note that CSM was the only
 221 campaign for which this criterion was not applied, as smoke was the sole focus of the mission and the flights are
 222 considered to all have been influenced to some extent. Moreover, CSM is unique amongst the campaigns examined
 223 where the scientific hypotheses to be tested are not as applicable due to the widespread smoke coverage, but we still
 224 examine it as it can provide useful insights.

225 Mann-Whitney U tests were performed for the aircraft data and the CW data, where the null hypotheses ($p \leq$
226 0.05) were that the medians of certain variables (N_s , N_n , wind speed and direction) and species concentrations of
227 southerly and northerly wind days were similar within a campaign.

2.2 Wind Direction Classification

230 To determine boundary layer wind direction in the study region, we used a number of data products, as each
231 provided unique advantages either related to temporal, spatial, or vertical coverage. Data from NOAA's National Data
232 Buoy Center (NDBC) were analyzed to verify the ocean surface wind direction was between 135° and 225° , which is
233 considered southerly in this study. We focused on wind direction during 1400 - 2200 UTC to overlap with when the
234 majority of RFs occurred (Marina, CA is 7 hours behind UTC). Other days classified as northerly flow adhered to
235 surface wind direction between 315° and 45° . Five buoys were used to match the ones used in Juliano et al. (2019a):
236 46011 (Santa Maria: 34.94° N, 120.99° W), 46013 (Bodega Bay: 38.24° N, 123.32° W), 46014 (Point Arena: 39.23°
237 N, 123.98° W), 46028 (Cape San Martin: 35.77° N, 121.90° W), and 46042 (Monterey: 36.79° N, 122.40° W). Buoy
238 locations relative to the CA coast are shown in Fig. 1 of Juliano et al. (2019a).

239 ~~We used Multi-Channel RGB data from the Geostationary Operational Environmental Satellite-WEST Full Disk
240 Cloud Product (GOES-15) at time resolutions of every three hours for E-PEACE, hourly for NiCE, BOAS, FASE,
241 and MACAWS, and every half hour for CSM. Wind direction was assessed via cloud movement, which was partly a
242 focus of this study (e.g., boundary layer cloud characteristics) with particular attention paid to the principal RF time
243 period. We investigated all days within a campaign month, and not just days coinciding with a RF. For example, E-
244 PEACE comprised flights from 9 July to 18 August 2011, and thus GOES data from 1 July through 31 August 2011
245 were investigated for that year.~~

246 The National Oceanic and Atmospheric Administration (NOAA) Hybrid Single-Particle Lagrangian Integrated
247 Trajectory (HYSPLIT; Stein et al., 2015; Rolph et al., 2017) model was ~~also~~ used to obtain back trajectories based on
248 North American Mesoscale Forecast System (NAM) meteorological data (12 km resolution) ending at Marina, CA
249 (36.67° N, 121.60° W; white diamond in Fig. 1) for 500, 900, 2,500, and 4,500 m AGL. Marina, CA was selected as
250 the ending point for the back-trajectories as this was the takeoff/landing location for all six campaigns. These altitudes
251 were selected to both capture marine boundary layer (MBL) and free troposphere (FT) winds and reflect the variety
252 of altitudes the Twin Otter aircraft flew at during the six campaigns in Table 1; however, the trajectories at 500 m
253 were most important for connecting to the aircraft data analysis.

254 For Twin Otter flight days, aircraft wind data were used to confirm that wind direction was either southerly or
255 northerly in the lowest 800 m of the flights (over ocean and land), which was the altitude range of most of the flight
256 time. For a case-by-case basis, archived surface weather charts were accessed via the NOAA Weather Prediction
257 Center (WPC) to investigate wind direction at specific sites (like Pt. Reyes).

258 ~~We also used Multi-Channel RGB data from the Geostationary Operational Environmental Satellite-WEST Full
259 Disk Cloud Product (GOES-15) to investigate cloud motion on northerly and southerly flow days. The analysis utilized
260 time resolutions of every three hours for E-PEACE, hourly for NiCE, BOAS, FASE, and MACAWS, and every half-
261 hour for CSM. We investigated all days within a campaign month, and not just days coinciding with a RF. For example,
262 E-PEACE comprised flights from 9 July to 18 August 2011, and thus GOES data from 1 July through 31 August 2011
263 were investigated for that year. While not an exact tracer for air motion, we did observe that clouds tended to follow
264 the prevalent air motion, particularly on southerly flow days.~~

2.3 NAAPS and COAMPS

267 Both the Navy Aerosol Analysis and Prediction System (NAAPS; Lynch et al., 2016;
268 <https://www.nrlmry.navy.mil/aerosol/>) and the Coupled Ocean/Atmosphere Mesoscale Prediction System (COAMPS;
269 Hodur, 1997) are used to support the analysis of airborne data collected during the six Twin Otter campaigns and
270 assess how well they can simulate southerly flow on days when observational datasets indicate such flow directions
271 offshore of CA. NAAPS is a global aerosol forecast model run by the U.S. Naval Research Laboratory (NRL) in
272 Monterey, CA that predicts 3-dimensional anthropogenic and biogenic fine (ABF), dust, sea salt, and biomass burning
273 smoke particle concentrations in the atmosphere. NAAPS relies on meteorological data derived from the Navy Global
274 Environmental Model (NAVGEM; Hogan et al., 2014) and considers 25 vertical levels in the troposphere. For this
275 study, we utilized the reanalysis version of NAAPS (NAAPS-RA, hereafter called NAAPS) that assimilates aerosol

276 depth observations to get a general sense of the simulated differences between southerly and northerly flow days for
277 our region of focus and as a complement to the aircraft data.

278 The motivation for the usage of these models is two-fold. The NAAPS-RA has a coarse horizontal resolution;
279 however, it provides large-scale aerosol conditions with observational constraints on the model fields (i.e.,
280 incorporates satellite retrieved aerosol optical depth). It is important to have this relatively accurate large-scale aerosol
281 background information for regional aerosol-cloud interaction research, as some of the background aerosol
282 information (e.g., biomass burning smoke) and pollution are advected into the interested study area. Another minor
283 reason is for model evaluation purposes: to see if models with different resolutions can resolve the studied phenomena,
284 as this is less studied and is of interest to check if models have the capability to represent them. The use of NAAPS
285 and COAMPS provides insight into how aerosol-cloud interactions from in situ data are represented by coarse
286 resolution models.

287 We investigated data for northward wind speed (v_{wind} , where northward (i.e., southerly) flow is indicated by
288 positive values) and mass concentrations for ABF aerosols and sea salt (Fig. 2), along with smoke, dust, coarse aerosol,
289 and fine aerosol (Fig. S2). Note that ABF represents secondarily formed species (SO_4^{2-} and secondary organic aerosol)
290 and primary organic aerosol generally within the fine mode ($<1 \mu\text{m}$). ~~To approximate~~ To be approximately similar to
291 the average boundary layer height of all the missions used in this study, the first five vertical levels (max height of
292 $\sim 668 \text{ m}$ above sea level) of NAAPS were used for data analysis. Vertical profiles of temperature for each campaign
293 categorized by flow regime are provided in Fig. S3 using aircraft data over the ocean, to show the general structure of
294 the lower troposphere in relation to the first five vertical levels of NAAPS.

295 For our analysis, the NAAPS data were first separated into southerly and northerly flow days for each campaign
296 based on results from Sect. 2.2, and the average value of each parameter was calculated for four reported times: 0000,
297 0600, 1200, and 1800 UTC. The most focus is placed on 1800 UTC, as that time coincided with most Twin Otter
298 flight periods (results for the remaining time periods are in Fig. ~~S3-S9S4-S10~~). Then, all the parameters except v_{wind}
299 were summed across the five vertical levels to get a total mass concentration ($\mu\text{g m}^{-3}$) up to $\sim 668 \text{ m}$ above sea level,
300 whereas the average was calculated for v_{wind} . Those values were used to calculate the difference between southerly
301 and northerly flow days at $1.0^\circ \times 1.0^\circ$ spatial resolution.

302 COAMPS is a high-resolution meteorological forecast model developed by the NRL's Marine Meteorology
303 Division (MMD) that outputs parameters like air temperature, winds, precipitation, cloud base and top heights, and
304 mass concentrations for the same aerosol species as those in NAAPS. For this study, we assessed the wind
305 speed/direction and smoke from COAMPS and NAAPS for the purpose of contrasting with observational data.
306 COAMPS maps were generated for this study by NRL at three different resolutions: 45 km, 15 km, and 5 km. To
307 compare to NAAPS, 15 km resolution grids were used. To assess the efficacy of COAMPS and NAAPS at forecasting
308 heavy pollution on a day with southerly winds, we performed a comparison of the two models for CSM RF 6 at 1800
309 UTC to match the flight time. The focus areas for both COAMPS and NAAPS matched that of the aircraft data
310 mentioned in Sect. 2.1.1. The altitudes used for the COAMPS maps for wind speed/direction and smoke were 762 m
311 and ~~305660~~ m, respectively, as the best match to the NAAPS maximum altitude used in this work.

313 2.4 IMPROVE

314 To investigate the difference in surface-level aerosol measurements between southerly and northerly flow days,
315 this study utilized composition data from the Interagency Monitoring of Protected Visual Environments (IMPROVE)
316 network (Malm et al., 1994; <http://views.cira.colostate.edu/fed/>). Data were taken from the Pt. Reyes National
317 Seashore surface station (38.07° N , 122.88° W) for the full campaign months shown in Table 1. Every third day,
318 gravimetric mass of particulate matter ($\text{PM}_{2.5}$ and PM_{10}) was measured. The $\text{PM}_{2.5}$ fraction was further analyzed via
319 ion chromatography and X-ray fluorescence (XRF) for water-soluble ions and elements, respectively, along with
320 organic and elemental carbon (OC and EC).

321 This study specifically investigated ($\mu\text{g m}^{-3}$): $\text{PM}_{2.5}$, coarse mass ($\text{PM}_{\text{coarse}} = \text{PM}_{10} - \text{PM}_{2.5}$), Cl^- , NO_3^- , SO_4^{2-} , Ni ,
322 K^+ , Si , V , EC, OC, and fine soil. The total OC measurement comes from a summation of four fractions of OC, which
323 are categorized by a method of carbon analysis detection temperature (e.g., Chow et al., 1993; Watson et al., 1994).
324 This method quantifies methane produced via volatilization of particulate species in pure helium at 120°C (OC1),
325 250°C (OC2), 450°C (OC3), and 550°C (OC4). Similarly, the total EC measurement is a summation of three fractions
326 categorized via combustion temperatures in a 98% pure helium and 2% pure oxygen environment: 550°C (EC1),
327 700°C (EC2), and 800°C (EC3). Fine soil concentrations are calculated as follows (Malm et al., 1994):

328
 329
$$\text{Fine soil } (\mu\text{g m}^{-3}) = 2.2 \times [\text{Al}] + 2.49 \times [\text{Si}] + 1.63 \times [\text{Ca}] + 2.42 \times [\text{Fe}] + 1.94 \times [\text{Ti}] \quad (2)$$

 330

331 This equation was confirmed by several studies (e.g., Cahill et al., 1981; Pitchford et al., 1981; Malm et al., 1994)
 332 through comparisons of resuspended soils and ambient particles.

333 Upon examination, it was decided to only use data for E-PEACE and BOAS because those campaign periods
 334 had more than a single point with valid data for southerly days (three and two, respectively); recall that IMPROVE
 335 data are only available every third day [due to the sample collection procedure](#), so some southerly days would not
 336 necessarily have available IMPROVE data. All the species analyzed had a status flag of “V0” (“Valid value”) or “V6”
 337 (“Valid value but qualified due to non-standard sampling conditions”), which are both considered valid data. We chose
 338 to include data flagged as “V6” (Cl, NO₃, and SO₄²⁻ for BOAS) due to the small quantity of usable data for southerly
 339 days. Additional information, like sampling protocols, are provided elsewhere
 340 (<http://vista.cira.colostate.edu/Improve/sops/>). Like the aircraft and CW data, Mann-Whitney U tests were performed
 341 on this dataset to determine if the median species concentrations were equivalent for southerly and northerly days
 342 across a campaign.
 343

344 2.5 MODIS

345 To assess cloud characteristics of southerly and northerly flow days during the campaign months of this study,
 346 we retrieved daily mean values within the same focus region defined for aircraft data in Sect. 2.1.1 (35.31° N – 40.99°
 347 N, 125.93° W – 118.98° W) for the following properties from the MODerate resolution Imaging Spectroradiometer
 348 (MODIS) on Aqua through NASA Giovanni (<https://giovanni.gsfc.nasa.gov/giovanni/>): cloud effective particle radius
 349 (r_e ; μm), cloud liquid water path (LWP; g m^{-2}), cloud optical thickness (COT), cloud fraction (from cloud mask), and
 350 aerosol optical depth (AOD, combined dark target and deep blue at 0.55 μm for land and ocean). N_d (cm^{-3}) was
 351 calculated from MODIS properties based on the following equation (Painemal and Zuidema, 2011):

352
$$N_d = 1.4067 \times 10^{-6} [\text{cm}^{-0.5}] \times \frac{\text{COT}^{0.5}}{r_e^{2.5}} \quad (3)$$

353 Additionally, retrieval data were only used when cloud fraction $\geq 30\%$ to maximize both data reliability and sample
 354 size (Mardi et al., 2021). The focus of the analysis is comparing median values of these remotely sensed variables
 355 between southerly and northerly days for E-PEACE and BOAS due to a similar LWP value for the two flow regimes
 356 (66.48/67.17 g m^{-2} and 84.40/89.90 g m^{-2} , respectively). Data for the other campaigns are included in the SI.
 357 Additionally, this study used MODIS visible imagery on NASA Worldview to qualitatively identify smoke plumes,
 358 in addition to fire radiative power from the MODIS Fire Information for Resource Management System (FIRMS;
 359 <https://earthdata.nasa.gov/firms>).
 360

361 3 Results and Discussion

362 3.1 Lower Tropospheric Wind Profile

363 We first examine NAAPS and airborne observations for the lower tropospheric wind profile during the
 364 periods of analysis shown in Table 1. Note that the other datasets described in Sect. 2.2 are consistent with the airborne
 365 wind results and thus only NAAPS and aircraft data are discussed here for two reasons: NAAPS results are used to
 366 assess how such a model quantifies differences in winds between southerly and northerly flow days as identified with
 367 methods in Sect. 2.2, whereas aircraft data provide insight into typical wind speeds during southerly and northerly
 368 flow periods.

369 Beginning with the aircraft data, results are discussed here only for measurements over the ocean with the
 370 $N_{d>10\text{nm}}$ filter applied to remove smoke influence (Table 3). The mode of wind directions during southerly and northerly
 371 flow days in each campaign expectedly aligned with southerly (144° – 194°) and northerly flow (327° – 332°),
 372 respectively, because of how the classification was done (Sect. 2.2). Median wind speeds across each campaign ranged
 373 from 2.35 – 7.75 m s^{-1} for southerly flow in contrast to 5.12 – 8.87 m s^{-1} for northerly flow. This finding differs from
 374 what has been observed in previous studies, likely due to the difference in sampling location: aircraft observations
 375 from the surface to 800 m versus buoy/surface observations, respectively. All campaigns featured higher median wind
 376 speeds for northerly flow flights. [However, when looking at the vertical wind profiles of each campaign for southerly](#)
 377 [and northerly flow days \(Fig. S11\), there were several instances where median wind speed at the surface for southerly](#)

378 flow days was greater than for northerly flow days. Both the median wind speeds and directions of southerly and
 379 northerly days were significantly distinct from one another for all of the studied campaigns (Table S4).

380
 381 **Table 3: Median values (southerly/northerly) of various parameters over the ocean with an $N_{a>10nm}$ filter such that RFs with**
 382 **median $N_{a>10nm} > 7,000 \text{ cm}^{-3}$ were removed from the final analysis to eliminate smoke interference. Mode values are used**
 383 **for wind direction. The instruments used for the parameters from left to right are as follows: CPC 3010, CPC 3010 –**
 384 **PCASP- $<1\mu\text{m}$, PCASP- $<1\mu\text{m}$, PCASP- $>1\mu\text{m}$, CPC 3025/CPC 3010, CASF. The far right-hand columns indicate the number of**
 385 **datapoints used from each campaign, with n_{Na} indicating the amount of data used for all N_a calculations, n_{Nd} is for cloud**
 386 **data, and n_{Wind} is for wind speed and direction. FSSP data were used for N_a data only during BOAS, whereas CASF was**
 387 **used in other campaigns. These data are for the lowest 800 m above sea level. The reader is referred to Fig. S10S12 for box**
 388 **plots corresponding to the analysis in this table, as well as Table S4 for Mann-Whitney U p-values.**

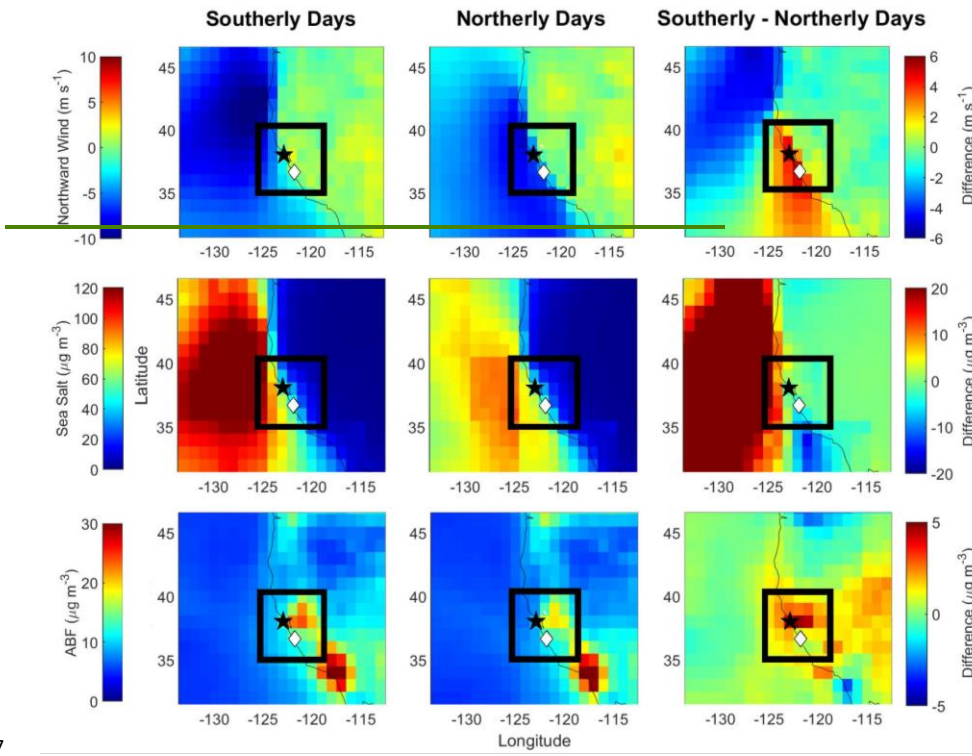
	$N_{a>10nm}$ (cm^{-3})	$N_{a10-100nm}$ (cm^{-3})	$N_{a0.1-1\mu\text{m}}$ (cm^{-3})	$N_{a>1\mu\text{m}}$ (cm^{-3})	$N_{a3};N_{a10}$ (-)	N_d (cm^{-3})	Wind Speed (m s^{-1})	Wind Direction ($^\circ$)	n_{Na} ($\times 10^3$)	n_{Nd} ($\times 10^3$)	n_{Wind} ($\times 10^3$)
E-PEACE	861 / 703	501 / 454	338 / 197	0 / 1.25	1.09 / 1.10	252 / 163	3.38 / 7.58	177.61 / 330.48	20.3 / 202.7	17.1 / 127.1	37.4 / 330.8
NICE	953 / 606	248 / 245	471 / 260	2.51 / 0	1.12 / 1.17	249 / 254	3.80 / 5.12	180.81 / 327.20	1.4 / 66.8	1.5 / 39.6	3.0 / 112.8
BOAS	750 / 497	553 / 256	204 / 196	0 / 1.24	1.20 / 1.18	143 / 127	5.49 / 6.35	166.97 / 328.58	5.8 / 72.1	3.9 / 20.5	11.8 / 104.7
FASE	836 / 916	423 / 635	326 / 180	0 / 0	1.29 / 1.16	203 / 223	2.35 / 6.82	144.03 / 331.29	1.0 / 95.5	0.3 / 99.2	1.3 / 194.9
MACAWS	722 / 815	560 / 635	154 / 164	0 / 0	1.25 / 1.26	189 / 165	7.75 / 8.87	162.15 / 330.28	10.3 / 118.9	6.6 / 27.0	16.9 / 145.9
CSM	5,558 / 3,451	5,081 / 3,366	515 / 365	1.00 / 0	1.30 / 1.67	334 / 314	6.10 / 6.77	193.93 / 332.16	4.8 / 31.5	1.8 / 4.1	6.9 / 41.3

	$N_{a>10nm}$ (cm^{-3})	$N_{a10-100nm}$ (cm^{-3})	$N_{a0.1-1\mu\text{m}}$ (cm^{-3})	$N_{a>1\mu\text{m}}$ (cm^{-3})	$N_{a3};N_{a10}$ (-)	N_d (cm^{-3})	Wind Speed (m s^{-1})	Wind Direction ($^\circ$)	n_{Na} ($\times 10^3$)	n_{Nd} ($\times 10^3$)	n_{Wind} ($\times 10^3$)
E-PEACE	861 / 703	501 / 454	338 / 197	0 / 1.25	1.09 / 1.10	252 / 163	3.38 / 7.58	177.61 / 330.48	20.3 / 202.7	17.1 / 127.1	37.4 / 330.8
NICE	953 / 606	248 / 245	471 / 260	2.51 / 0	1.12 / 1.17	249 / 254	3.80 / 5.12	180.81 / 327.20	1.4 / 66.8	1.5 / 39.6	3.0 / 112.8
BOAS	750 / 497	553 / 256	204 / 196	0 / 1.24	1.20 / 1.18	143 / 127	5.49 / 6.35	166.97 / 328.58	5.8 / 72.1	3.9 / 20.5	11.8 / 104.7
FASE	836 / 916	423 / 635	326 / 180	0 / 0	1.29 / 1.16	203 / 223	2.35 / 6.82	144.03 / 331.29	1.0 / 95.5	0.3 / 99.2	1.3 / 194.9
MACAWS	722 / 815	560 / 635	154 / 164	0 / 0	1.25 / 1.26	189 / 165	7.75 / 8.87	162.15 / 330.28	10.3 / 118.9	6.6 / 27.0	16.9 / 145.9
CSM	5,558 / 3,451	5,081 / 3,366	515 / 365	1.00 / 0	1.30 / 1.67	334 / 314	6.10 / 6.77	193.93 / 332.16	4.8 / 31.5	1.8 / 4.1	6.9 / 41.3

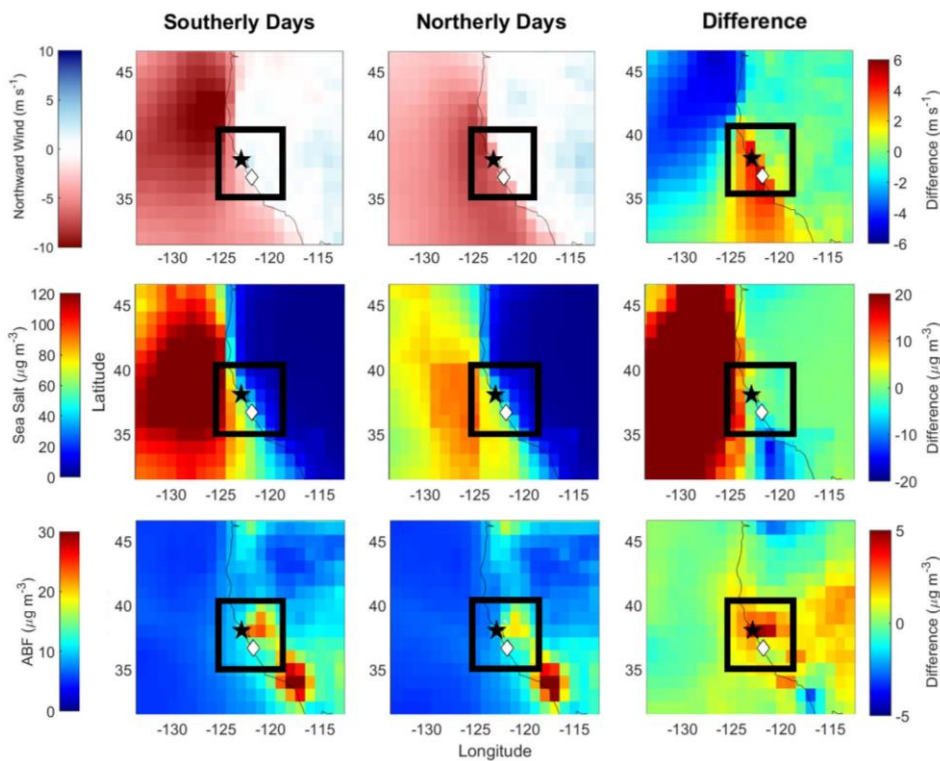
391
 392 For context, boundary layer flow patterns from NAVGEM are provided in Fig. S13 for all southerly and
 393 northerly days at 1800 UTC (Fig. S14 and S15 provide flow maps for each individual campaign). The average
 394 southerly flow pattern (Fig. S13a) captures generally weaker flow, particularly near Marina, CA, where a slight
 395 reversal can be observed. When looking at the flow maps for each campaign (Fig. S14 and S15), only BOAS and
 396 FASE captured a small wind reversal by Marina, CA during southerly flow days. Both MACAWS and CSM had a
 397 circulatory-pattern north of Marina, CA, near Pt. Reyes, and southerly flow is more clearly observed during the CSM
 398 campaign along the coast.

399 NAAPS values are discussed for v_{wind} for the lowest ~668 m above sea level, with positive (negative) values
 400 representing southerly (northerly) flow (Fig. 2). This altitude range coincides with the airborne data shown in Table
 401 3. The v_{wind} data are categorized into “Southerly Days,” “Northerly Days,” and “~~Southerly—Northerly~~
 402 ~~Days~~” “Difference” (i.e., southerly – northerly values) for 1800 UTC, which overlaps with most of the Twin Otter flight
 403 times (Fig. 1); results for 0000, 0600 and 1200 UTC are provided in Fig. S3S4. Both southerly and northerly days had
 404 less negative weaker v_{wind} closer to the coast (up to 35° N) compared to farther offshore over the ocean (~ $-3/-9$ and -
 405 $4/-6 \text{ m s}^{-1}$, respectively, for southerly/northerly flow). Slower Slow, slightly northerly winds extended farther north to
 406 Marina and west to 123.5° W for southerly days, which is illustrated in red (differences exceeding $\sim 3 \text{ m s}^{-1}$ between
 407 flow regimes) in the “~~Southerly—Northerly Days~~” panel. Northerly days also had an area of less
 408 negative weaker v_{wind} north of 43.5° N , which is emphasized in the “~~Southerly—Northerly Days~~” panel in
 409 blue (differences of $-4 - -6 \text{ m s}^{-1}$). NAAPS was not able to fully capture southerly winds over the ocean and along the
 410 coast in that v_{wind} was not clearly positive (i.e., not northward); however, the magnitude of the wind speed difference
 411 along the coastal area of the study domain appeared to align with the mechanics of coastal wind reversal and CTDs:
 412 the weakening of northerly wind and ultimate reversal of flow (e.g., Winant et al., 1987; Melton et al., 2009). A key

413 conclusion from NAAPS is that the difference between southerly and northerly flow days matches expectations with
414 southerly days having at least a greater tendency towards more positive higher v_{wind} compared to northerly days, but
415 still not necessarily distinctly positive v_{wind} values.
416



417



418
 419 **Figure 2:** Average northward wind speed (v_{wind} ; m s^{-1}), total sea salt mass concentration ($\mu\text{g m}^{-3}$), and total ABF mass
 420 concentration ($\mu\text{g m}^{-3}$) of campaign months at 1800 UTC for 1st through 5th NAAPS levels (up to ~ 668 m above sea level)
 421 for southerly and northerly flow wind days. The right-most panel illustrates the difference between southerly and northerly
 422 flow days. The airbase in Marina, CA is denoted by a white diamond, Pt. Reyes is indicated with a black star, and the black
 423 box indicates the region of focus in this study.

425 3.2 Aerosol Response to Southerly Flow

426 3.2.1 Fire Radiative Power Maps

427 Prior to discussing aerosol results, we address the influence of wildfire emissions, which is an aerosol
 428 source that varies in terms of strength between the six campaign periods in contrast to shipping and other forms of
 429 continental emissions that are more consistent year to year. Past studies using airborne and surface-based data at
 430 Marina, CA (airbase indicated by a white diamond in Fig. 1 and 2) overlapping with the six campaigns in Table 1
 431 revealed the following in terms of notable biomass burning influence around Marina and offshore areas (e.g.,
 432 Prabhakar et al., 2014; Braun et al., 2017; Mardi et al., 2018): (i) E-PEACE/BOAS: no major influence of note; (ii)
 433 NiCE: influence around the last week of July 2013; (iii) FASE: influence between 25 July and 12 August; (iv)
 434 MACAWS: significant influence on flights during 28 June and 3 July owing to the aircraft having flown close to
 435 wildfire areas inland in northern CA; (v) CSM: significant influence throughout the campaign. These archived notes
 436 do not preclude the possibility of biomass burning influence during other periods of those campaigns as it relates to
 437 Twin Otter aerosol and cloud measurements.

438 Spatial maps of fire radiative power (FRP; Fig. 3), indicative of burn intensity, show relatively less burning
 439 activity in immediate proximity to Marina during E-PEACE and BOAS. In contrast, the other campaigns show
 440 clusters of burning spots around Marina. Note that CSM, by virtue of its name, was focused largely on wildfires
 441 with dedicated RFs to sample smoke. MACAWS also was designed as a wildfire study but had less cases of strong

Formatted: Normal (Web), Left

442 plumes to sample, which included RFs on 28-29 June farther inland than most RFs, resulting in very high aerosol
443 number concentrations ($N_{a>10nm} > 10,000 \text{ cm}^{-3}$). These maps are mainly contextual to show the spatial distribution of
444 fire sources and specific conclusions cannot be gleaned solely based on these regarding which campaigns had more
445 or less wildfire influence overlapping with the flight tracks. This is especially the case because smoke can be
446 advected from far distances away from the study region. The wildfire filter described in Sect. 2.1 aims to filter out a
447 large portion of smoke influence, at least at the regional level.
448

449 3.2.2 Fine Aerosol

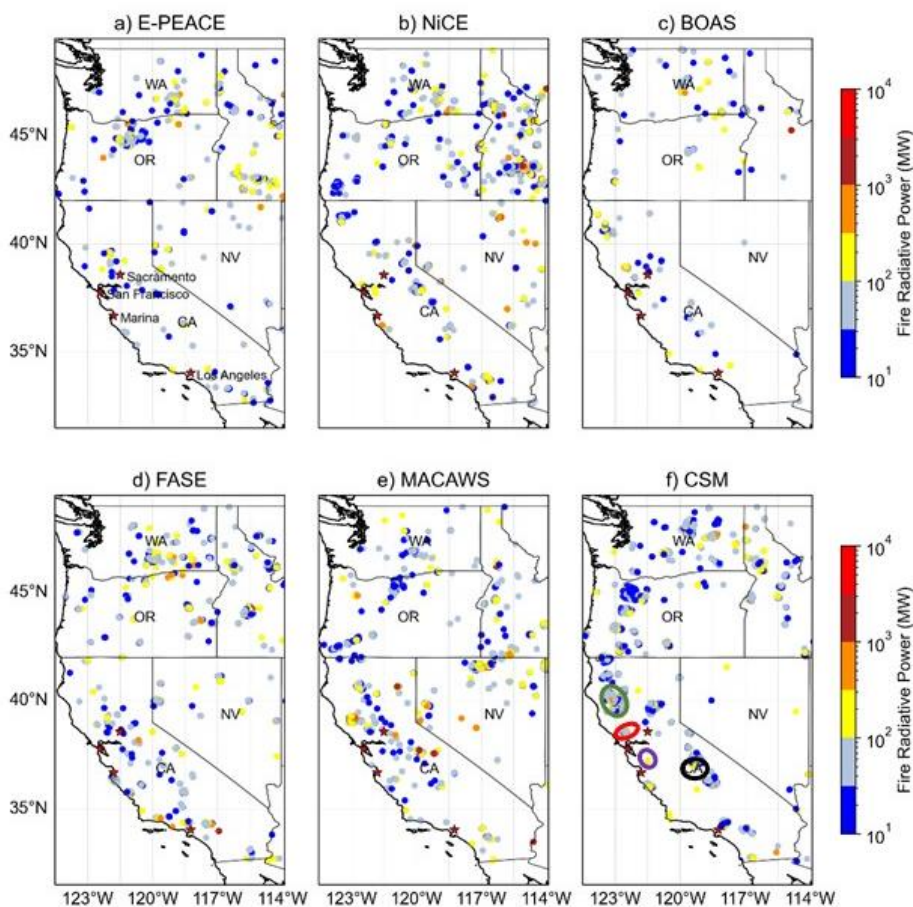
450 The first hypothesis of this study is that southerly flow yields higher fine aerosol levels associated with
451 anthropogenic and continental tracer species due to more perceived influence from land and shipping sources (Juliano
452 et al., 2019a; 2019b). This was also speculated by Hegg et al. (2008) although it was not examined in great detail by
453 that study. Here we rely on results from a number of datasets including measurements from the Twin Otter (Tables 3
454 and 4) and the Pt. Reyes IMPROVE site (Fig. 4), along with NAAPS model results (Fig. 2).
455

456 3.2.2.1 Airborne: Particle Concentration

457 Beginning with the Twin Otter data, aerosol data for 17 southerly flight days corresponding to 21 RFs were
458 compared to 93 other flight days with predominantly northerly flow in Table 3 (box plots of the variables [are](#) in Fig.
459 [S10S12](#), and Mann-Whitney U test results are in Table S4), as well as Tables S1-S3. We focus primarily on flight data
460 over the ocean with the $N_{a>10nm}$ filter applied to omit wildfire influence; the other aircraft data result tables in the
461 Supplement generally show the same trends as Table 3. We caution that the results of FASE, and to a slightly lesser
462 extent NiCE, are not as meaningful as the other campaigns owing to the least amount of [statistics data](#) for southerly
463 conditions, with numbers of datapoints shown in the tables.

464 The total submicron aerosol number concentration, $N_{a>10nm}$, was far larger for southerly flow ($722\text{-}5,558 \text{ cm}^{-3}$)
465 as compared to northerly flow flights ($497\text{-}3,451 \text{ cm}^{-3}$). Of the six campaigns, the only ones with higher median
466 values in northerly flow were FASE and MACAWS, with small $\Delta N_{a>10nm}$ of -80 cm^{-3} and -93 cm^{-3} , respectively. CSM
467 exhibited the largest difference in median values for $N_{a>10nm}$ between southerly and northerly flow ($\Delta N_{a>10nm} = 2,107$
468 cm^{-3}), followed by NiCE ($\Delta N_{a>10nm} = 347 \text{ cm}^{-3}$) and BOAS ($\Delta N_{a>10nm} = 253 \text{ cm}^{-3}$). While these campaigns have a
469 smaller relative sample size of southerly data ($n_{Na} < 6 \times 10^3$; CSM: 4.8×10^3 , NiCE: 1.4×10^3 ; and BOAS: 5.8×10^3), E-
470 PEACE has a sizable amount of southerly data (20.3×10^3) and the least fire influence of the missions included in this
471 study, so we find it may be the most reliable campaign to analyze. There was a distinct difference between southerly
472 and northerly days during E-PEACE as well, with a $\Delta N_{a>10nm}$ of 158 cm^{-3} . As the number concentration in the
473 submicron range dominates the total CPC concentrations, these results convincingly point to an enhancement of fine
474 aerosol pollution in southerly flow even without the $N_{a>10nm}$ filter (Table S1).

475 We examined various size ranges of particles in the submicron range as well. For particles between 10-100
476 nm, southerly conditions generally had higher number concentrations except again for FASE and MACAWS and with
477 more comparable levels during NiCE. As particles larger than 100 nm are more relevant for cloud condensation nuclei
478 (CCN) activity, we also examined number concentrations for diameters between 0.1 and $1 \mu\text{m}$, which show higher
479 southerly levels except for MACAWS. Between campaigns, CSM overall exhibited the highest particle concentrations
480 in this size range due to extensive wildfire emissions in the area, which are known to be linked with enhanced levels
481 of particles larger than 100 nm in the same region (Mardi et al., 2018), which is why this campaign shows relatively
482 large PCASP enhancements in both southerly and northerly flow conditions relative to the other campaigns (see in
483 particular Tables S1-S2). Without the CPC filter (Table S1), only the medians for NiCE and BOAS on northerly wind
484 days changed, resulting in the $N_{a10-100nm}$ median during NiCE to be lower during southerly flow days compared to
485 northerly days. When looking within the region of focus, the inclusion of land data in addition to ocean data (Tables
486 S2-S3) leads to significant N_a differences (to a lesser extent for the filtered data, Table S3) compared to Table 3,
487 including higher submicron concentrations for NiCE, BOAS, and FASE.
488



489 Figure 3: Spatial maps of fire radiative power (FRP), downloaded from the MODIS Fire Information for Resource
 490 Management System (FIRMS; <https://earthdata.nasa.gov/firms>) for the entire months spanning individual field
 491 campaigns in Table 1. Only FRP values with a high detection confidence level ($\geq 80\%$) are shown (Giglio et al., 2015). The
 492 circled areas in panel (f) correspond to some of the largest wildfires in CA state history that occurred in 2020 that are
 493 referred to in Sect. 3.4.2: August Complex fire (green), SCU Lightning Fire Complex (purple), Creek fire (black), and
 494 LNU Lightning Complex fire (red).
 495

496
 497 Although new particle formation (NPF) was not expected to be prominent in the lower 800 m owing mostly
 498 to high aerosol surface areas especially due to sea spray emissions, we still examined the ratio of N_a above 3 nm
 499 relative to 10 nm ($N_{a3}:N_{a10}$), as this ratio is a commonly used marker for identifying NPF. Such instances are more
 500 common in the free troposphere in the study region owing to reduced aerosol surface areas (Dadashazar et al., 2019).
 501 The results suggest that the $N_{a3}:N_{a10}$ ratios for the two flow regimes were significantly different for all the campaigns
 502 except for MACAWS (higher ratios in southerly flow for BOAS and FASE), with median flow direction-dependent

503 values per campaign ranging from 1.09 to 1.30. During CSM, the median ratio value was 1.67 in northerly flow
 504 conditions due to presumed influence from high precursor levels in smoke plumes.

505
 506 **3.2.2.2 Airborne: Tracer Species in Cloud Water**

507 We next turn to CW composition data (Table 4) to continue learning more about the effect of southerly flow
 508 and its associated emission sources. NiCE and FASE were not included in the CW calculations of Table 4 (but shown
 509 in Fig. S4S16) because there were fewer than five samples from RFs with southerly wind direction for those two
 510 campaigns, and CW was not collected during CSM. NO₃⁻ and nss-SO₄²⁻, both representative of fine aerosol pollution,
 511 were higher for southerly days, with a significant difference (Table S5) apparent in E-PEACE (1.80/0.30 and 2.10/0.81
 512 μg m⁻³ for southerly and northerly days, respectively), as well as for NO₃⁻ during BOAS (1.02/0.23 μg m⁻³ for southerly
 513 and northerly days, respectively). The same trend was observed for V (ship exhaust tracer) and NH₄⁺, which can be
 514 used as a tracer for continental sources such as agriculture (Juliano et al., 2019b). Thus, these results help to provide
 515 more confidence in results from Juliano et al. (2019b) but with increased statisticsampling across more campaigns.
 516 For E-PEACE and MACAWS, there were also lower southerly flow concentrations of K⁺ (0.01/0.05 and 0.06/0.11 μg
 517 m⁻³) and Ca²⁺ (0.05/0.07 and 0.06/0.16 μg m⁻³), suggestive of less influence from biomass burning and dust sources
 518 with the caveat that K⁺ and Ca²⁺ have sources other than biomass burning and dust.

519 There were also higher concentrations of oxalate during southerly days, which can be used as a tracer for aqueous
 520 processing (Hilario et al., 2021), wherein cloud droplets are formed from oxidized volatile organic compounds (Ervens
 521 et al., 2011; Ervens, 2015; McNeill, 2015). Further, there were significant differences in median concentrations
 522 between southerly and northerly flow days during BOAS and MACAWS (0.12/0.05 and 0.08/0.03 μg m⁻³,
 523 respectively). Precursors to oxalate are diverse including from biogenic sources, biomass burning, combustion (e.g.,
 524 Stahl et al., 2020 and references therein), shipping, along with being associated with sea salt and dust owing to gas-
 525 particle partitioning (Sorooshian et al., 2013; Stahl et al., 2020; Hilario et al., 2021); such sources are presumed to be
 526 influential during southerly flow based on the notion that air masses are influenced by some combination of continental
 527 emissions and extended time in shipping lanes.

528 Cloud water pH was lower and thus more acidic on southerly days for all three campaigns (3.85/4.54, 4.30/4.34,
 529 4.33/4.62 for southerly/northerly days during E-PEACE, BOAS, and MACAWS, respectively, and statistically
 530 different for E-PEACE and BOAS), which is another indicator for anthropogenic pollution enriched with acidic
 531 species (Pye et al., 2020). Increased acid levels can result in more Cl⁻ depletion when considering sea salt particles
 532 (e.g., Edwards et al., 2023 and references therein); interestingly, southerly days were characterized by lower Cl⁻:Na⁺
 533 ratios with median values of 1.39 (MACAWS), 1.63 (E-PEACE) (both campaigns of which southerly days were
 534 significantly different from northerly flow days), and 2.48 (BOAS), although the difference in MACAWS was only
 535 0.12. Braun et al. (2017) noted that, theoretically, over 60% of the Cl⁻ depletion in the submicron range could be
 536 attributed to nss-SO₄²⁻, and greater than 20% in the supermicron range could be attributed to NO₃⁻. As was noted
 537 previously, nss-SO₄²⁻ and NO₃⁻ were noticeably enhanced during southerly flow days while the Cl⁻:Na⁺ ratios were
 538 reduced. Schlosser et al. (2017) also reported that organic acids, notably oxalate, were significantly enhanced during
 539 periods of Cl⁻ depletion, which is reflected in our CW data. As E-PEACE was statistically the most robust dataset (and
 540 all CW species except Ca²⁺, NH₄⁺, and oxalate had medians that were significantly different between southerly and
 541 northerly flow days), the results from CW convincingly align with more shipping and/or continental influence in
 542 southerly flow to impact cloud composition.

543
 544 **Table 4: Median values (southerly/northerly) of water-soluble CW composition (μg m⁻³) over the entirety of three**
 545 **campaigns with sufficient data. The starred (*) values are reported in ng m⁻³. The number of samples used in each campaign**
 546 **is in the far-right hand column (n). The reader is referred to Table S5 which shows the p-values from the Mann-Whitney**
 547 **U tests, as well as Fig. S4S16 which shows box plots of the CW composition results for the five campaigns with available**
 548 **data. Values shown as “—” denote when samples were below the limit of detection.**

	Ca ²⁺	Cl ⁻ :Na ⁺	K ⁺	Na ⁺	NH ₄ ⁺	NO ₃ ⁻	Oxalate	pH	nss-SO ₄ ²⁻	V	n
E-PEACE	0.05/0.07	1.63/2.15	0.01/0.05	0.42/1.21	—/—	1.80/0.30	0.02/0.02	3.85/4.54	2.10/0.81	2.16*/0.38*	10/65
BOAS	0.11/0.08	2.48/2.74	0.06/0.06	1.99/1.55	0.44/0.04	1.02/0.23	0.12/0.05	4.30/4.34	1.08/0.83	—/0.15*	5/21
MACAWS	0.06/0.16	1.39/1.51	0.06/0.11	1.30/2.70	0.08/0.05	0.55/0.38	0.08/0.03	4.33/4.62	0.56/0.26	0.07*/0.05*	15/51

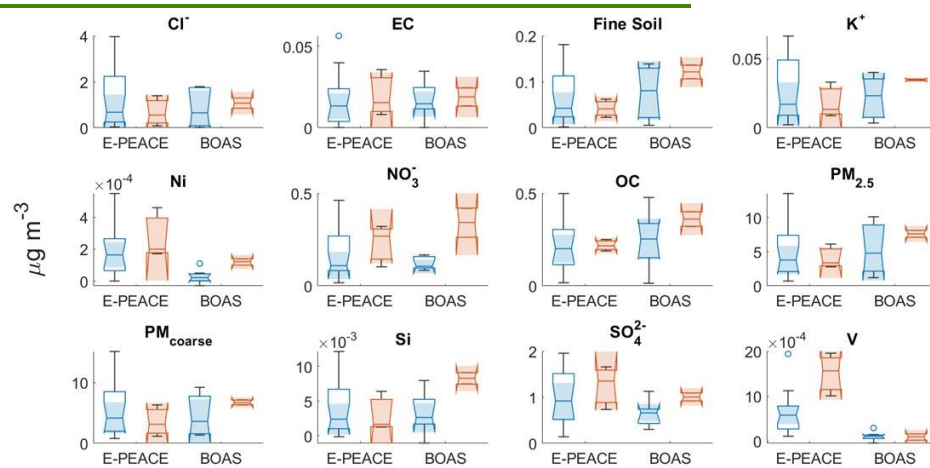
549

	Ca^{2+}	Cl^-/Na^+	K^+	Na^+	NH_4^+	NO_3^-	Oxalate	pH	ms-SO_4^{2-}	V	n
E-PEACE	0.05 / 0.07	1.63 / 2.15	0.01 / 0.05	0.42 / 1.21	— / —	1.80 / 0.30	0.02 / 0.02	3.85 / 4.54	2.10 / 0.81	2.16* / 0.38*	10 / 65
BOAS	0.11 / 0.08	2.48 / 2.74	0.06 / 0.06	1.99 / 1.55	0.44 / 0.04	1.02 / 0.23	0.12 / 0.05	4.30 / 4.34	1.08 / 0.83	— / 0.15*	5 / 21
MACAWS	0.06 / 0.16	1.39 / 1.51	0.06 / 0.11	1.30 / 2.70	0.08 / 0.05	0.55 / 0.38	0.08 / 0.03	4.33 / 4.62	0.56 / 0.26	0.07* / 0.05*	15 / 51

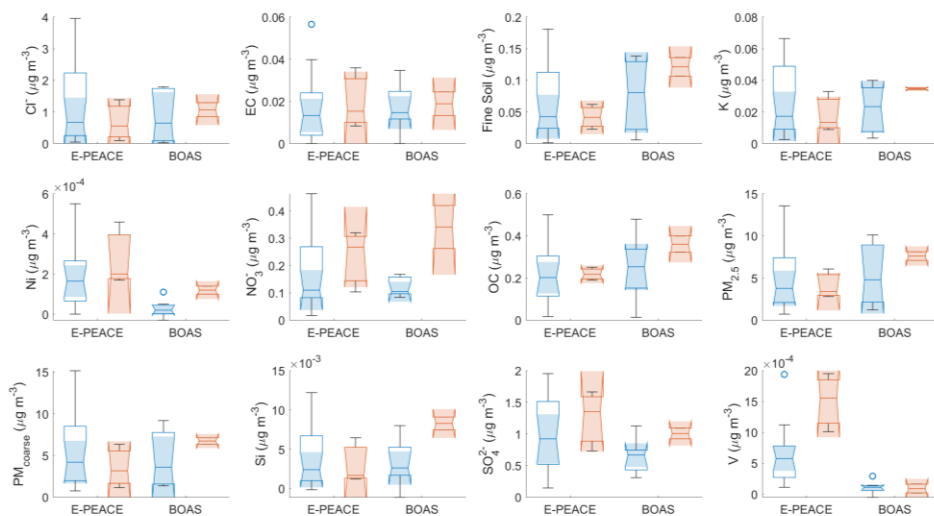
550

551 3.2.2.3 Surface: Aerosol Composition

552 We next examine surface composition data from the Pt. Reyes IMPROVE site. Mass concentrations of twelve
 553 PM composition variables were investigated to analyze important tracers along the coast (Fig. 4), with Mann-Whitney
 554 U test p-values for comparing southerly and northerly flow days shown in Table S6. It is important to recall that E-
 555 PEACE and BOAS were the only campaigns that had more than a single day of valid data coinciding with southerly
 556 flow because of the added challenge of IMPROVE sampling occurring every third day; therefore, northerly days had
 557 significantly more data points (18 for E-PEACE and seven for BOAS) compared to southerly days (three and two,
 558 respectively). That is the general reason for the large whiskers on the box plots for northerly RFs during E-PEACE
 559 and the lack of whiskers for southerly RFs during BOAS. Another feature to note is the ‘folded over’ appearance of
 560 some of the box plots. This indicates a high variance within the dataset and a skewed distribution. We caution that this
 561 analysis is not very statistically robust owing to the rare nature of southerly days in overlap with IMPROVE sampling;
 562 however, we take a ‘better than nothing’ approach to use in a supportive role in comparison to other datasets used to
 563 assess differences between southerly and northerly flow.
 564



565



566
 567 **Figure 4: Box plots of IMPROVE data from the Pt. Reyes surface station. The southerly data for E-PEACE and BOAS**
 568 **(three and two points, respectively) are represented by the red boxes, and the northerly data (18 and seven, respectively)**
 569 **are represented by the blue boxes.**

570
 571 SO_4^{2-} , NO_3^- , OC, V, Ni, and EC are reasonable tracer species representative of either shipping and/or continental
 572 sources in the study region, as they have been utilized as tracers for these sources in previous studies (Wang et al.,
 573 2014; Maudlin et al., 2015; Wang et al., 2016; Dadashazar et al., 2019; Ma et al., 2019). These species were
 574 hypothesized to be more enhanced in the coastal CA zone on southerly flow days due to air spending time over
 575 shipping lanes and land upwind of the study region. Even with the limited southerly flow statistessample data, the
 576 results of Fig. 4 support this idea as southerly conditions coincide with higher median concentrations of these species
 577 than northerly days. The most striking relative differences were for NO_3^- (southerly/northerly): 0.27/0.11 and 0.34/0.10
 578 $\mu\text{g m}^{-3}$ for E-PEACE and BOAS, respectively. NO_3^- was the only species during BOAS that was found to have a
 579 median concentration that was statistically different between southerly and northerly days (Table S6). Ni and V are
 580 the primary trace metals in heavy ship fuel oils and are commonly used as tracers for ship emissions (Celo et al., 2015;
 581 Corbin et al., 2018), and V was previously found enhanced in CW linked to ship emissions in E-PEACE (Coggon et
 582 al., 2012; Prabhakar et al., 2014). There were mostly higher concentrations of these species on southerly flow days
 583 (E-PEACE southerly/northerly: 0.20/0.17 and 1.56/0.58 ng m^{-3} , respectively; BOAS southerly/northerly: 0.12/0.02
 584 and 0.09/0.11 ng m^{-3} , respectively), supporting the hypothesis of elevated shipping emissions. Also, a Mann-Whitney
 585 U test found that the median V concentrations during E-PEACE were statistically different for southerly and northerly
 586 days (Table S6).

587 Only BOAS exhibited higher $\text{PM}_{2.5}$ during southerly days compared to northerly days (7.61/4.82 $\mu\text{g m}^{-3}$,
 588 respectively), with E-PEACE having roughly equivalent concentrations for the two flow regimes (3.39/3.78 $\mu\text{g m}^{-3}$,
 589 respectively). This is likely owing to how $\text{PM}_{2.5}$ is not the best marker for shipping and continental emissions owing
 590 to its inclusion of other species of marine and natural origin.

591
 592 **3.2.2.4 NAAPS: Aerosol Composition**

593 To round out discussion of fine aerosol pollution, we discuss NAAPS model results (Fig. 2). The largest
 594 enhancements in ABF mass concentrations occurred inland both north of Marina around Pt. Reyes and near the Ports

595 of Los Angeles and Long Beach. There was $>5 \mu\text{g m}^{-3}$ difference in ABF concentration between southerly and
596 northerly days near Pt. Reyes. This suggests that while there were elevated levels of anthropogenic emissions in this
597 area regardless of the flow regime, there were increased concentrations during southerly flow days according to
598 NAAPS. An example HYSPLIT back-trajectory for a southerly flow day (Fig. S17) shows air masses with likely
599 influence from as far south as southern California and the U.S.-Mexico border. Additionally, there is a strong ABF
600 signal ($>30 \mu\text{g m}^{-3}$) around 34°N , 118°W for both categories of days, which is close to the Ports of Los Angeles and
601 Long Beach, two of the busiest container ports (in terms of cargo volume processed) in the United States and areas
602 with elevated levels of NO_x and SO_x due to the ship exhaust and port emissions (Corbett and Fischbeck, 1997). As
603 can be seen in the Fig. S56, the ABF concentrations around 34°N , 118°W and 38°N , 122°W increase throughout
604 the day, with more significant increases north of the ports for southerly flow days. On southerly flow days, NAAPS
605 results point to marked enhancements in fine aerosol and smoke mass concentration north of Pt. Reyes over water but
606 with mostly a reduction in such values to the south of Pt. Reyes over water. ABF represents the category of species
607 that are most tied to the tracer species shown already to be enhanced in southerly flow, and thus at least this result
608 from NAAPS is consistent with enhanced values across most of the study domain in southerly flow.
609

610 3.2.3 Supermicron Aerosol

611 While this study hypothesizes that most of the aerosol changes in southerly flow will pertain to submicron
612 aerosol, we still discuss supermicron aerosol characteristics to determine if there was any change observed. With all
613 the complexities leading to sea salt emissions in the region (Schlosser et al., 2020), which is the predominant
614 supermicron aerosol type in the study region's boundary layer, combined with the shifting wind directions and speeds
615 leading up to and after a wind reversal (e.g., Juliano et al., 2019a), there was no underlying expectation for a change
616 in levels during southerly flow events. Beginning with the aircraft observations, $N_{\text{a}>1\mu\text{m}}$ levels were generally low and
617 usually zero in terms of flight median values simply due to so many zero values during a RF. Northerly flow conditions
618 yielded median levels exceeding zero for E-PEACE (1.25 cm^{-3}) and BOAS (1.24 cm^{-3}). In contrast, southerly flow led
619 to levels of 2.51 cm^{-3} and 1.00 cm^{-3} during NiCE and CSM, respectively. The enhancement during southerly flow
620 during at least CSM is presumed to be due to pervasive smoke during many of those RFs. However, the small median
621 concentrations for each campaign make it hard to definitively determine if the lower concentrations during E-PEACE
622 and BOAS were due to changes in flow regime or another factor. Figure S1 shows a scatterplot of total CASF number
623 concentration versus effective diameter to separate out where cloud droplets are relative to probable sea salt particles
624 and then coarse aerosol associated with the wildfires. There is considerable data coverage at $\text{LWC} < 0.02 \text{ g m}^{-3}$, with
625 effective diameters below $5 \mu\text{m}$ and number concentrations exceeding 10 cm^{-3} , with the latter surpassing what would
626 be expected from sea salt (e.g., Gonzalez et al., 2022). It is very likely that dust particles can be entrained into regional
627 smoke plumes as discussed in past work for the region (e.g., Maudlin et al., 2015; Schlosser et al., 2017). This will be
628 discussed in more detail for a case flight demonstrating such high levels during southerly flow in Sect. 3.4.2.

629 Airborne CW results reveal generally no strong trends in either sea salt or dust tracer species between the flow
630 regimes. The sea salt tracer species Na^+ was lower for southerly days during E-PEACE (and statistically different)
631 and MACAWS ($0.42/1.21$ and $1.30/2.70 \mu\text{g m}^{-3}$ for southerly/northerly days) but with an increase during BOAS (1.99
632 versus $1.55 \mu\text{g m}^{-3}$). The dust tracer species Ca^{2+} was, expectedly, much less abundant compared to Na^+ , without
633 significant differences between flow regimes. However, as already noted (Sect. 3.2.2.2), the fine pollution in southerly
634 flow likely still influenced supermicron aerosol characteristics via Cl^- depletion in salt particles.

635 In terms of IMPROVE data, $\text{PM}_{\text{coarse}}$, Si, fine soil, and Cl^- are the variables that would best coincide with
636 typical sources of supermicron aerosol (i.e., dust and sea salt). They did not reveal any consistent trend for the two
637 campaigns. Based on the lack of a general trend and limited/reduced data for southerly statistics flow days, it is
638 concluded that there is insufficient evidence from IMPROVE to conclude that there is more or less dust or salt
639 influence on southerly days.

640 The wind profile discussed in Sect. 3.1 has implications for sea salt aerosol production, which is influenced by
641 wind speed. The breaking of wave crests to produce (mostly coarse mode) spray droplets occurs at strong wind
642 conditions ($>10 \text{ m s}^{-1}$) (Monahan et al., 1986). Additionally, jet droplets are produced via bubble bursting at lower
643 wind speeds ($>5 \text{ m s}^{-1}$; Blanchard and Woodcock, 1957; Fitzgerald, 1991; Wu, 1992; Moorthy and Satheesh, 2000).
644 On southerly days, there were faster northerly winds over the open ocean offshore west of 125°W , which
645 corresponded to high sea salt concentrations ($>100 \mu\text{g m}^{-3}$) according to NAAPS, whereas northerly days had slower
646 v_{wind} and less sea salt ($65 - 90 \mu\text{g m}^{-3}$) in those same areas farther offshore. In contrast, in the coastal areas south of

647 35° N, northerly days had higher sea salt concentrations (by 10 – 20 $\mu\text{g m}^{-3}$) than southerly days with weaker (less
648 negative) v_{wind} . NAAPS shows the same general trends for coarse aerosol mass compared to sea salt, with dust being
649 far less abundant and more spatially heterogeneous in terms of enhancements and reductions between southerly and
650 northerly conditions. In general, the NAAPS results are consistent with aircraft and IMPROVE results in that in the
651 study domain, there was not any pronounced difference in coarse aerosol characteristics during southerly flow. [More](#)
652 [research and data would be helpful, though, to put this conclusion on firmer ground.](#)

653

654 3.3 Cloud Responses

655 3.3.1 Airborne In Situ Results

656 As most campaigns exhibited higher N_a on southerly flight days, it matches expectation that most campaigns
657 exhibited higher N_a values for southerly days (southerly/northerly values): E-PEACE (252/163 cm^{-3}), BOAS (143/127
658 cm^{-3}), MACAWS (189/165 cm^{-3}), and CSM (334/314 cm^{-3}). These campaigns had southerly N_a values that were ~
659 $20 \pm 4 \text{ cm}^{-3}$ greater than the median values on northerly days, with a significant difference during E-PEACE ($\Delta N_a \sim$
660 89 cm^{-3}). E-PEACE also had the [bestmost](#) cloud data [statisticspoints](#) compared to the other missions, qualifying it as
661 the most robust campaign for inspection of cloud properties. The remaining two campaigns had the least amount of
662 cloud data during southerly flow conditions (NiCE and FASE) and thus those results are of less importance to discuss.
663 CSM had the highest N_a concentrations for both southerly and northerly days due to the strongest levels of pollution
664 (from smoke) relative to the other campaigns.

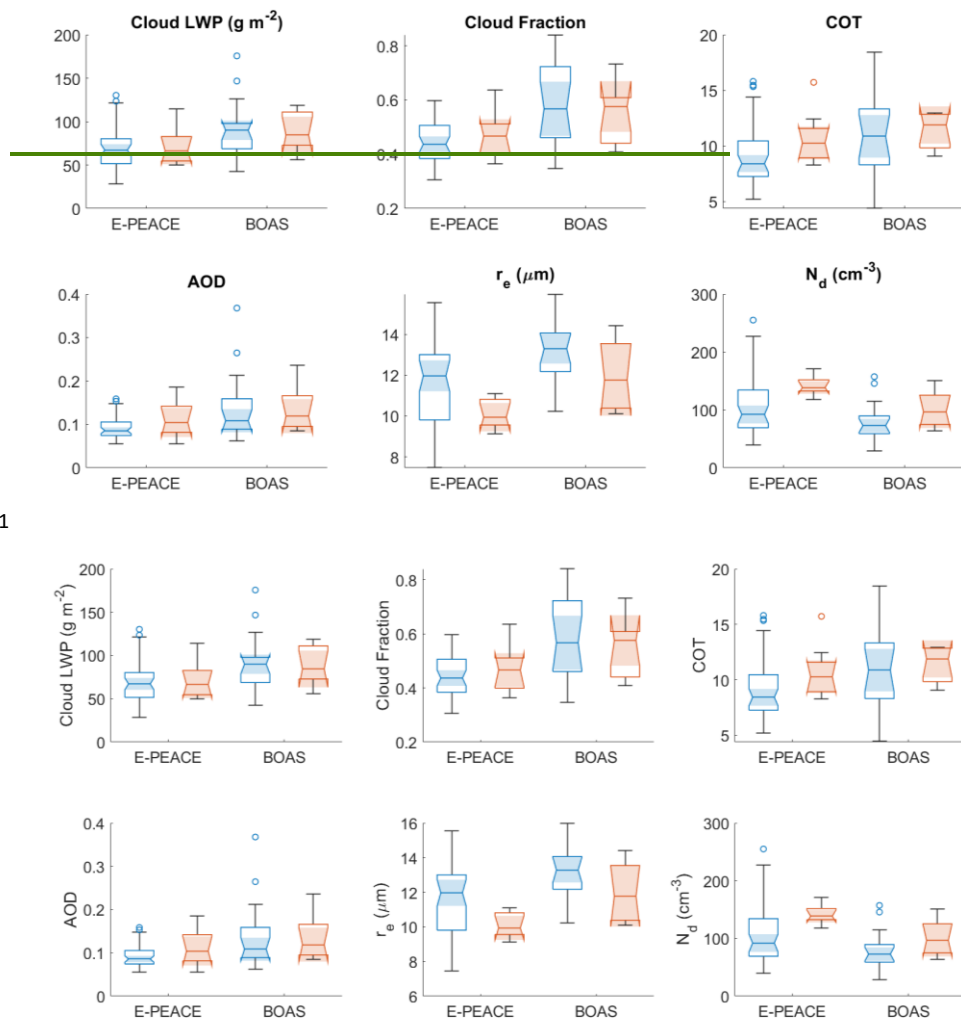
665

666 3.3.2 Satellite Data Results

667 The second part of our hypothesis was that there would be a noticeable difference in cloud properties like N_d , r_e ,
668 and COT between southerly and northerly flow days (at fixed LWP), namely due to the change in emissions sources.
669 In particular, we anticipated higher N_d and COT and lower r_e for southerly flow periods due to the Twomey effect
670 (Twomey, 1974) and higher particle concentrations from continental pollution and shipping emissions. Six parameters
671 were retrieved from MODIS, divided into southerly and northerly days for E-PEACE and BOAS, and visualized as
672 box plots (Fig. 5). Cloud LWP medians for southerly and northerly days within E-PEACE (66.48/67.17 g m^{-2}) and
673 BOAS (84.40/89.90 g m^{-2}) were not significantly different. Therefore, these two campaigns are the focus here, unlike
674 the other campaigns that had larger differences (Table S7). The medians for N_d were higher for southerly days
675 (138.54/91.99 cm^{-3} and 96.59/72.80 cm^{-3} for southerly/northerly wind days during E-PEACE and BOAS,
676 respectively), and the southerly and northerly medians during E-PEACE were significantly different from one another.
677 Consistent with the Twomey effect (Twomey, 1974), the median r_e for southerly flow days was lower than northerly
678 flow days (9.94/11.97 μm and 11.77/13.29 μm), with the medians during E-PEACE being significantly different.
679 Cloud optical thickness was also higher for southerly days compared to northerly days for both campaigns (10.27/8.42
680 and 11.88/10.87 for E-PEACE and BOAS, respectively); however, the medians for each flow regime were not found
681 to be significantly different from one another. We note that even NiCE with LWP values being slightly higher for
682 southerly days (82.78 g m^{-2} versus 74.54 g m^{-2}), the same general results are observed with southerly days having
683 higher N_d /COT and reduced r_e (Table S7); the other three campaigns did not follow these N_d /COT/ r_e trends due to the
684 larger LWP differences between flow regimes.

685 Although no differences were necessarily expected, we still examined cloud fraction and AOD, which were
686 similar within a campaign for the two types of days (0.47/0.44 versus 0.58/0.57, and 0.10/0.09 versus 0.12/0.11,
687 respectively, for southerly and northerly wind days during E-PEACE versus BOAS). Based on these results, N_d , r_e ,
688 and COT differences between flow regimes match our hypothesis, and two out of the three parameters during E-
689 PEACE were found to be significantly different between southerly and northerly days.

690



691

692

693 Figure 5: Box plots of MODIS data within the study region during the periods overlapping with E-PEACE and BOAS. The
 694 southerly data for E-PEACE and BOAS (eight points each) are represented by the red boxes, and the northerly data (44
 695 and 17 points, respectively) are represented by the blue boxes. The notches (and shading, which helps to more clearly
 696 indicate where the notches end) of the boxes assist in the determination of significance between multiple medians. If the
 697 notches overlap, the medians are not significantly different from one another.
 698

699

3.4 Case Studies

700

In addition to looking at whole campaigns, we also looked closely at two RFs with southerly wind direction:
 701 NiCE RF 16 (29 July 2013) and CSM RF 6 (10 September 2020). NiCE RF 16 was a unique flight, which coincided

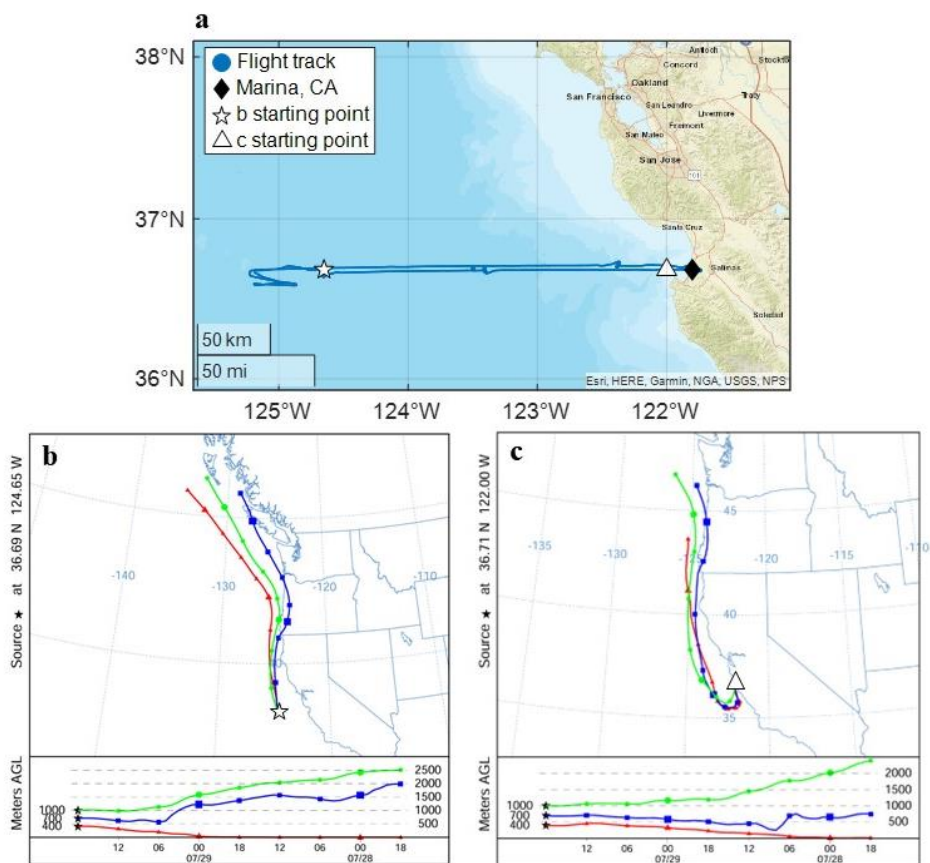
702 with a CTD event (Bond et al., 1996; Nuss, 2007) and its flight path extended past 125° W into a large stratocumulus
703 cloud clearing (Crosbie et al., 2016; Dadashazar et al., 2020), which was unusual for the Twin Otter flights. CSM RF
704 6 was on a heavily polluted day owing to biomass burning emissions during one of the worst wildfire periods in CA
705 history. These case studies help emphasize the complexity of flow patterns in the region that influence the ability of
706 aerosols from different sources to arrive at the boundary layer in the study region. The observed changes in aerosol
707 and cloud properties between northerly and southerly days are likely not due to an instant switch in flow direction but
708 rather there is critical nuance in the timing, strength, and duration of the wind reversal, along with likely influence
709 from free tropospheric aerosol which can be sourced from various continental areas across California and even farther
710 away (Dadashazar et al., 2019).

711

712 3.4.1 NiCE Research Flight 16

713 NiCE RF 16 (29 July 2013) occurred on a day with a large stratocumulus cloud deck clearing, which, at its
714 widest point, was 150 km (Crosbie et al., 2016). As noted in Crosbie et al. (2016), this was a CTD event during the
715 time of the flight, and the boundary layer wind reversal (and resulting northwesterly flow) occurred under the
716 stratocumulus cloud deck within 100 km of the coast (~ 36.7° N, 123° W). The location of the wind reversal was
717 known, which allowed us to investigate if there was any apparent gradient in aerosol and cloud variables from the
718 coast to out over the ocean. The aircraft departed from Marina at approximately 1700 UTC, with a nearly straight,
719 westward path (Fig. 6a) toward the clear-cloudy boundary (reader is referred to Fig. 1a of Crosbie et al., 2016 for
720 boundary location). At the clear-cloudy interface (~ 36.7° N, 125° W, 1845 – 2000 UTC), stacked legs were performed
721 at multiple levels in both the MBL and FT on both sides of the boundary. Subsequently, the aircraft returned to Marina
722 following the initial outbound path. To visualize the location and general timing of the wind reversal (Fig. 6b-c), 48-
723 hr back-trajectories from HYSPLIT were used. This contrasts with the 24-hr back trajectories used to confirm
724 southerly wind flow in Sect. 2.2. For the case studies, 48-hr periods were used to have a better understanding of air
725 mass history. This case of southerly wind is one where the sampled air mass was likely to have spent more time in the
726 coastal area just south of Marina as compared to traditional northerly flow, where there was presumed influence from
727 shipping emissions and possibly advected continental air.

728

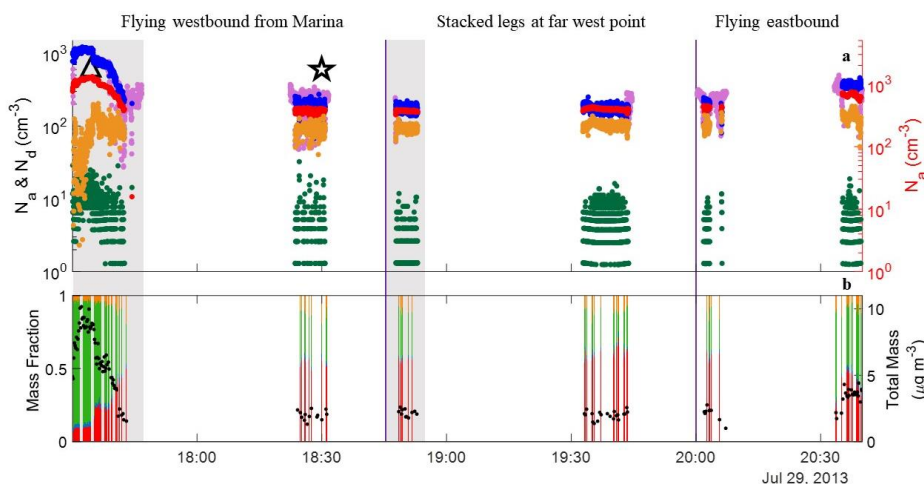


729
 730 **Figure 6:** (a) NiCE RF 16 (07/29/2013) flight track, with Marina represented by a solid black diamond, the starting point
 731 of the HYSPLIT back-trajectory in panel (b) indicated by a white star, and the starting point of the HYSPLIT back-
 732 trajectory in panel (c) indicated by a white triangle. (b) 48-hour back trajectory of a point (36.69° N, 124.65° W) along the
 733 flight path outside of the southerly wind zone (HYSPLIT end time: 1800 UTC). (c) 48-hour back trajectory of a point (36.71°
 734 N, 122.00° W) along the flight path at the beginning of the RF (HYSPLIT end time: 1700 UTC) where there was southerly
 735 flow. Panels (b) and (c) detail back-trajectories for three different altitudes: 400, 700, and 1000 m.
 736

737 We investigated gradients from the coast to farther offshore including past the wind reversal for several
 738 parameters, including N_a , N_d , and AMS total mass and mass fractions, both in the sub-cloud MBL (<525 m AGL, Fig.
 739 7) and in the FT (>765 m AGL, Fig. S42S18), both altitudes of which were defined in Crosbie et al. (2016). There
 740 was a general trend of decreasing number concentration, especially for $N_{a0.1-1\mu m}$, $N_{a>10nm}$, and N_d , from the coast to
 741 slightly before the stacked legs at the far west point (1,245/189, 1,240/390, and 772/263 cm^{-3} , respectively, at
 742 ~1732/1830 UTC). There was a wide range of supermicron concentrations for the whole flight duration, however,
 743 generally, there was a slight decrease of $N_{a>1\mu m}$ along the flight path going west as well, but it was not as pronounced
 744 as the other variables (24/4 cm^{-3}).

745 The eastbound leg to Marina was an interesting situation as there was no longer southerly flow closer to the
 746 coast yet there was still a concentration increase for number and cloud drop concentrations but not up to the same
 747 maximum levels that were observed on the westbound portion of the flight, probably owing to the reduced influence
 748 from areas south of the sampling area ($N_{a0.1-1\mu\text{m}}$: 248/435, $N_{a>10\text{nm}}$: 454/752, N_d : 272/434, and $N_{a>1\mu\text{m}}$: 5/19 cm^{-3} , for
 749 eastbound/westbound legs at ~2000/2037 UTC). AMS mass concentrations dropped significantly in the outbound
 750 portion of the flight, from total mass as high as $10.16 \mu\text{g m}^{-3}$ (~1730 UTC) to $1.55 \mu\text{g m}^{-3}$ (~1745 UTC), the latter of
 751 which was approximately 10 km offshore. During that period, organic mass fraction decreased from 0.81 to 0.28 in
 752 favor of growing SO_4^{2-} mass fraction from 0.11 to 0.50. On the inbound track, similar to N_a/N_d results, there was not
 753 as much of an enhancement in total mass (max of $4.41 \mu\text{g m}^{-3}$ at ~2040 UTC) and the chemical profile revealed more
 754 comparable levels of SO_4^{2-} and organic mass fractions (0.39 and 0.52, respectively, at ~2040 UTC) in contrast to the
 755 outbound track that showed higher organic mass fraction right by the coast.

756 The results suggest that the enhanced residence time of air masses (due to the wind reversal) in an area with
 757 presumed influence from shipping emissions (see Fig. 9 in Coggon et al., 2012) and continental pollution yielded an
 758 offshore gradient in N_a , N_d , and aerosol composition. Also, the results help show that this general coastal zone area in
 759 the location of the wind reversal is enhanced with fine pollution, which generally will affect aerosol and cloud
 760 characteristics if air masses spend prolonged time in it during southerly flow conditions. This all being said, it is hard
 761 to unambiguously attribute the aerosol and cloud changes to emissions from a particular area and source due to the
 762 complex flow nature in both the horizontal and vertical directions during the wind reversal period. This case study
 763 helps motivate continued research studying these events.
 764



765 **Figure 7: Data from NiCE RF 16 in the MBL (<525 m). The grey shading indicates time periods with mostly southerly**
 766 **winds, and the purple lines across all graphs indicate flight zones (outbound track, stacked legs at farthest west point, and**
 767 **inbound track). (a) The colored points on the left-hand axis correspond to $N_{a0.1-1\mu\text{m}}$ (blue, PCASP- $<1\mu\text{m}$), $N_{a>1\mu\text{m}}$ (green,**
 768 **PCASP- $>1\mu\text{m}$), and N_d (light purple, CASF). The colored points on the right-hand axis correspond to $N_{a>10\text{nm}}$ (red, CPC) and**
 769 **$N_{a10-100\text{nm}}$ (yellow, CPC 3010 – PCASP- $<1\mu\text{m}$). The triangle corresponds to the HYSPLIT back-trajectory end point seen in**
 770 **Fig. 6c, and the star corresponds to the HYSPLIT back-trajectory end point seen in Fig. 6b. (b) Stacked bar plot of AMS**
 771 **mass fractions of SO_4^{2-} (red), NO_3^- (blue), organics (green), and NH_4^+ (orange), overlaid with total mass concentration (μg**
 772 **m^{-3} ; black).**
 773
 774

775 The trends in the FT are much more ambiguous than those in the MBL (Fig. S12S18). Similar to the MBL,
 776 there was a decrease in $N_{a0.1-1\mu\text{m}}$ and $N_{a>10\text{nm}}$ from the coast to near the stacked legs (2,467/395 and 2,820/689 cm^{-3} ,
 777 respectively, at ~1726/1844 UTC), however there was no discernable trend for $N_{a>1\mu\text{m}}$. There were no apparent
 778 offshore trends for AMS total mass or speciated mass fractions. Additionally, on the eastbound flight leg, there was

779 not a clear trend for any of the parameters. This suggests that the effects of the southerly winds were stronger in the
780 MBL than the FT.

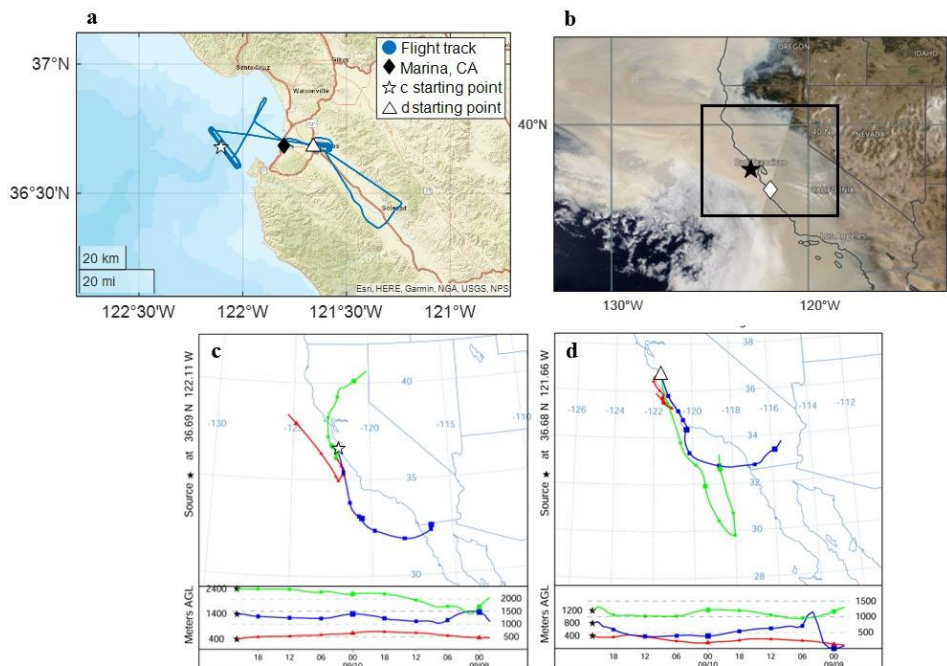
781

782 3.4.2 CSM Research Flight 6

783 CSM stands out among all of the examined campaigns owing to the strength and temporal persistence of
784 wildfire plumes, which was also the main focus of the mission. Of the top 3% ($n = 12$) of the largest fires in CA in the
785 historical record, four occurred in 2020 (circled in Fig. 3): the August Complex fire (16 August, Mendocino County),
786 the SCU Lightning Fire Complex (18 August, Santa Clara County), the Creek fire (4 September, Madera County),
787 and the LNU Lightning Complex fire (16 August, Hapa County) (Keeley and Syphard, 2021). These four fires were
788 a mix of both merged (August Complex) and unmerged (LNU Lightning Complex) fires that burned over 417, 160,
789 153, and 146 kha, respectively, and burned for months after they were ignited.

790 CSM RF 6 (10 September 2020) included two major components (Fig. 8a): a spiral over Salinas (max altitude
791 of 6,172 m at ~2000 UTC) and a spiral over Monterey Bay (max altitude of 4,822 m at ~2170 UTC). The entire region
792 was heavily impacted by smoke during CSM RF 6 (Fig. 8b). Additionally, around 36.5° N, 125° W, there is an area
793 not dominated by smoke, but rather, clouds, pointing to the likelihood of smoke-cloud interactions in the region on
794 not just this day but other CSM days with similar smoky conditions. HYSPLIT back-trajectories for the two spirals
795 for a 48-hr period were generated (Fig. 8c and 8d). For the spiral over Monterey Bay (Fig. 8c), the lowest altitude
796 trajectory (trajectory beginning at 400 m) is mostly northwesterly, the second lowest altitude (trajectory beginning at
797 1400 m) is primarily southerly, and the highest altitude (trajectory beginning at 2400 m) is approximately
798 northeasterly. The highest altitude back-trajectory passes over the LNU Lightning Complex fire (red oval; circled in
799 Fig. 3). For the spiral over Salinas (Fig. 8d), all three altitude levels (400, 800, and 1200 m AGL) reveal southerly
800 trajectory paths, and the air masses from the second-highest altitude back-trajectory possibly had some influence from
801 the SCU Lightning Fire Complex (purple oval) and the August Complex Fire (green oval) due to offshore and
802 northerly flow in the preceding 36-hr (Fig. 3).

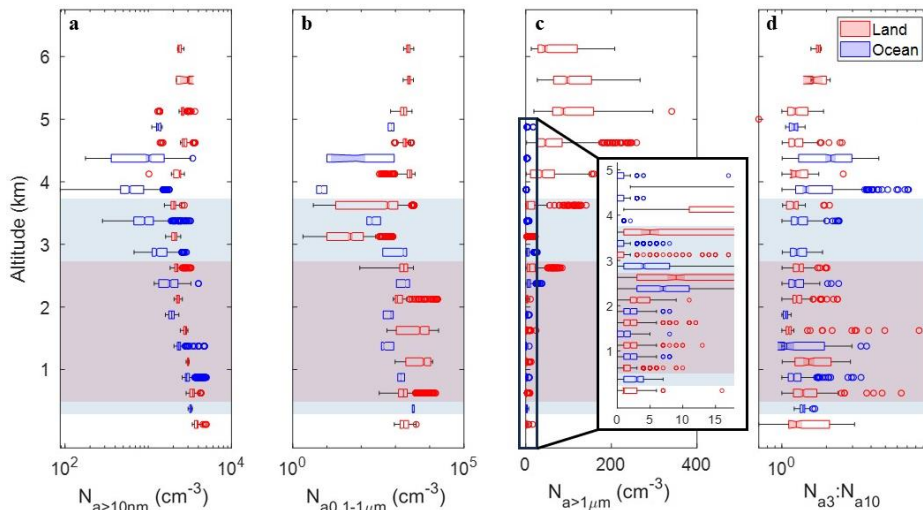
803



804 Figure 8: (a) CSM RF 6 (09/10/2020) flight track, with Marina, CA represented by a solid black diamond, the starting point
 805 of the HYSPLIT back-trajectory in panel (c) indicated by a white star, and the starting point of the HYSPLIT back-
 806 trajectory in panel (d) indicated by a white triangle. (b) NASA Worldview image, with Marina, CA represented by a white
 807 diamond, and Pt. Reyes denoted by a black star. (c) 48-hour back trajectory of a point (36.69° N, 122.11° W) along the flight
 808 path during the sounding over Monterey Bay (HYSPLIT end time: 2100 UTC) at three different altitudes: 400, 1400, and
 809 2400 m. (b) 48-hour back trajectory of a point (36.68° N, 121.66° W) along the flight path during the sounding over Salinas
 810 (HYSPLIT end time: 1900 UTC) at three different altitudes: 400, 800, and 1200 m. (c) and (d) utilized different altitudes
 811 for the back-trajectories to reflect the different maximum altitudes of the two major soundings of the flight.
 812

813
 814 The vertical profiles of temperature, wind speed, and wind direction are provided in Fig. S13S19 for context.
 815 Notably, the vertical region with southerly flow was thicker over the ocean (approximately 370 – 3700 m) versus over
 816 land (540 – 2900 m). N_a for different size ranges and $N_{a3}:N_{a10}$ are shown separately for land and over the ocean (Fig.
 817 9). There was more variability in $N_{a>10nm}$ (Fig. 9a) over the ocean, with a general decrease in concentration with
 818 increase in altitude for both data over land and ocean, followed by increasing $N_{a>10nm}$ above of the region of primarily
 819 southerly flow (non-shaded points)-the region of primarily southerly flow (non-shaded points). As illustrated by the
 820 composite boundary layer flow pattern in Fig. S15e-f, smoke along the coast during southerly flow periods was re-
 821 circulated northwest of Marina, CA nearby the flight path (which was not observed for the northerly composite flow
 822 pattern), which could have also influenced the elevated aerosol concentrations during this flight. There was not much
 823 change in $N_{a>1\mu m}$ (medians = 1 – 3 cm^{-3} ; range = 0 – 6 cm^{-3} ; Fig. 9c) until >2.5 km, where concentration increases over
 824 land (medians = 5 – 97 cm^{-3} ; range = 0 – 297 cm^{-3}) where there is primarily northerly flow, likely from sampling
 825 smoke plumes. Over the ocean, low supermicron particle concentrations are observed (≤ 7 cm^{-3}). These results show
 826 that during extensive smoky periods, the flow regime does not matter in cases like RF6 due to smoke generally being
 827 all across the region. Furthermore, the results show that supermicron particle concentrations are certainly enhanced in
 828 smoke plumes, as has been observed before in the study region (Mardi et al., 2018) but not to this pronounced extent,
 829 especially at high altitudes over land.

830 The $N_{a3}:N_{a10}$ ratio (Fig. 9d) was generally consistent over land across all vertical levels, with a good number
 831 of outliers in the region of primarily southerly flow. The medians of the ratios over the ocean were usually lower than
 832 the medians over land until 3.5 km. There was no discernable difference in the $N_{a3}:N_{a10}$ ratio over land between
 833 southerly and northerly flow (medians approximately 1.35 until >5.5 km) or over the ocean (medians for both flow
 834 regimes approximately 1.20, with a slight bump to 1.26 and 2.14 between 3.5 and 4.5 km). The reader is referred to
 835 Sect. S1 (Supplement) for discussion about NAAPS and COAMPS results for this case study as they relate to flow
 836 behavior and aerosol characteristics.
 837

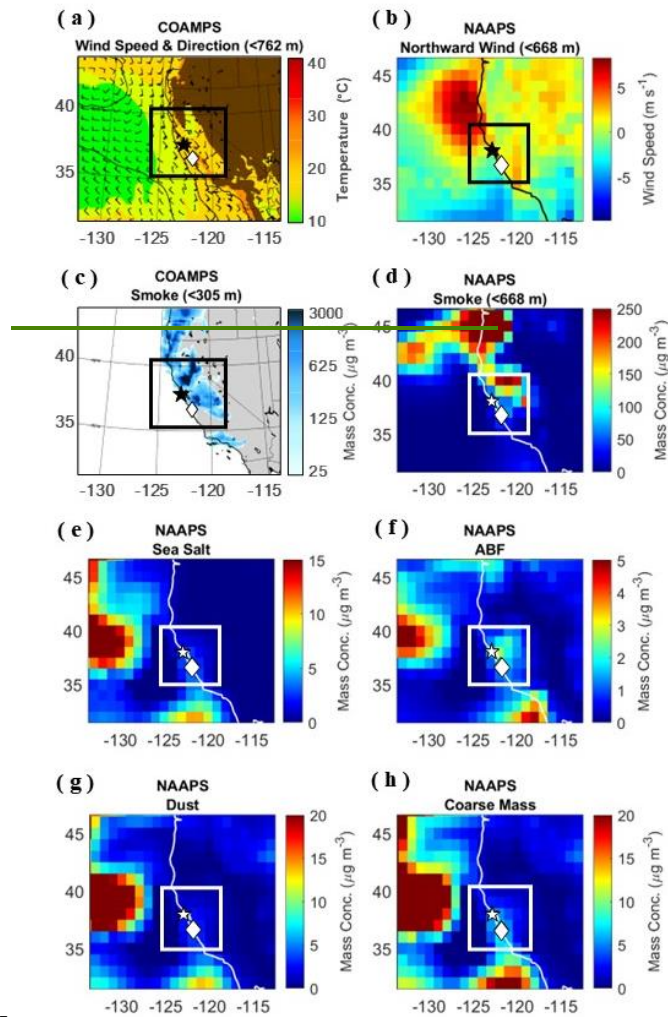


838
 839 **Figure 9:** CSM RF 6 box plot vertical profiles of (a) $N_{a>10nm}$ (cm^{-3}), (b) $N_{a0.1-1\mu m}$ (cm^{-3} ; PCASP $_{<1\mu m}$), (c) $N_{a>1\mu m}$ (cm^{-3} ;
 840 PCASP $_{>1\mu m}$), and (d) $N_{a3}:N_{a10}$. Data are shown every 500 m over land (red) and ocean (blue) above the MBL, which is the
 841 maximum altitude of the first bins for all the panels. Panel (c) has an additional focus on altitudes ≤ 5 km ($N_{a>1\mu m} \leq 18$
 842 cm^{-3}). The red and blue shading indicates altitudes over the land and ocean, respectively, with southerly winds.
 843

844 ——— Complementary data from NAAPS and COAMPS are shown in Fig. 10 for this case flight. COAMPS and
 845 NAAPS (Fig. 10a and 10b, respectively) both show southerly winds generally in the outlined study domain, which is
 846 consistent with observational data showing southerly winds close to Marina. NAAPS shows stronger southerly winds
 847 over land near Marina compared to over Monterey Bay whereas there was not much of a difference in wind speed
 848 between the two spiral soundings from the Twin Otter (Fig. S13). COAMPS better simulates southerly flow along the
 849 coastline, whereas the spatial resolution of NAAPS is probably a reason for it not being able to capture southerly flow
 850 in the grid spaces closest to the coast especially just south of Marina—instead there is weak northerly flow.

851 ——— A notable difference between NAAPS and COAMPS when it comes to modeling smoke (Fig. 10c and 10d,
 852 respectively) is that NAAPS better represents smoke over the ocean and more closely matches the visible satellite
 853 imagery from Fig. 8b. COAMPS does not capture smoke over the ocean away from the coastline. We do not focus on
 854 comparing absolute mass concentrations of smoke as it is difficult to know the ground truth value from the aircraft
 855 observations and also because of the different ways and size classifications for smoke in the two models. Generally,
 856 though, NAAPS and COAMPS match in the general areas identified as having smoke and areas of high concentrations
 857 match one another. Looking at Fig. 10e, NAAPS shows high concentrations of sea salt offshore west of 130° W.
 858 However, near the flight area and within our region of focus, sea salt concentrations are less than $5 \mu\text{g m}^{-3}$. NAAPS
 859 ABF (Fig. 10f) mirrors the areas with areas of high sea salt in Fig. 10e, but similar to model results from Sect. 3.2.2.4,
 860 there are areas of higher ABF concentrations ($2-3 \mu\text{g m}^{-3}$) near the ports of Los Angeles and Long Beach (34° N,

861 118° W) as well as up north near San Francisco and San Jose (38° N, 122° W). NAAPS dust (Fig. 10g) and coarse
 862 mass (Fig. 10h) also resemble the areas with high sea salt, with coarse mass concentrations exceeding $10 \mu\text{g m}^{-3}$ near
 863 both Marina, CA and Pt. Reyes.
 864



865
 866 **Figure 10:** COAMPS/NAAPS images are for 2100 UTC. (a) Wind speed and direction up to 762 m derived from COAMPS.
 867 The colors indicate surface temperature ($^{\circ}\text{C}$). (b) Wind speed of northward wind up to 668 m derived from NAAPS. (c)
 868 Smoke concentration ($\mu\text{g m}^{-3}$) up to 305 m derived from COAMPS. (d) Smoke, (e) sea salt, (f) ABF, (g) dust, and (h) coarse
 869 mass concentrations ($\mu\text{g m}^{-3}$) up to 668 m derived from NAAPS. The white diamond indicates Marina, CA, the white star
 870 indicates Pt. Reyes, and the black & white boxes indicate our zone of interest.
 871 **4 Conclusions**

872 In this study, we utilized multiple types of data, including a large repository of NPS Twin Otter data, to
873 compare coastal aerosol and cloud characteristics near central CA for northerly and southerly wind regimes in the
874 lower troposphere. Juliano et al. (2019a) had previously called for future studies to utilize in situ observations to
875 support their investigation into cloud properties using satellite observations. Our study is among the first to investigate
876 aerosol and cloud droplet number concentrations through in situ aircraft data in addition to CW composition, and
877 intercompare those results with satellite data, as well as models and surface station data. This builds upon previous
878 studies, such as Juliano et al. (2019b), by utilizing similar data sources in greater proportions.

879 Our first hypothesis is proven correct in that more fine aerosol pollution is present off the CA coast during
880 southerly flow due to likely influence from shipping exhaust and continental emissions including from major cities
881 like Los Angeles. We caution that there is considerable complexity in flow patterns both horizontally and vertically
882 when northerly winds change to southerly winds and this warrants more research to study for instance how influential
883 free tropospheric air is for the boundary layer aerosol changes occurring on southerly flow days. Submicron aerosol
884 pollution is found to be higher during southerly flow days (particularly during E-PEACE), with respect to both N_a
885 ($N_{a>10nm}$, $N_{a10-100nm}$, $N_{a0.1-1\mu m}$) and concentrations of shipping and continental tracer species in surface data (SO_4^{2-} , NO_3^-
886 , OC, V, Ni, and EC) and CW samples (nss- SO_4^{2-} , NO_3^- , NH_4^+ , V and oxalate). Cloud water is shown to be more acidic
887 during southerly flow along with more Cl^- depletion based on lower $Cl^-:Na^+$ ratios. A secondary hypothesis was that
888 increased influence from shipping and/or continental emissions would lead to enhanced N_d and COT and lower r_e (at
889 fixed LWP) due to the Twomey effect (Twomey, 1974). Both the airborne in situ data and satellite retrievals show
890 increased N_d on southerly days. The satellite retrieval data also reveal higher COT and lower r_e during southerly flow
891 The increase in N_d and decrease in r_e associated with the northerly to southerly reversal matches results of a previous
892 study in the region (Juliano et al., 2019a). The analysis of CSM RF 6 reveals that during heavy biomass burning
893 periods with prevailing smoke, there is relatively no difference in aerosol or cloud properties associated with changes
894 in flow regime. Based on the NAAPS evaluation, while coarse-gridded models can capture differences in wind
895 direction and aerosol concentration between southerly and northerly flow days, they are not fully able to reproduce
896 southerly flow.

897 A limitation in this type of study to address in the future is the difficulty of obtaining detailed in situ data
898 during southerly wind conditions. As noted already, wind reversals along coasts extend to a number of other global
899 regions (e.g., South America, southern Africa, Australia) and thus it is recommended to continue building more
900 statistics/increasing the sample data volume to better understand changes in aerosol and cloud properties as a function
901 of wind direction along coastal regions. Intercomparisons with models, as partly done here, can aid with determining
902 if model resolution should improve to better simulate these events. Generally speaking, the prevalence of fine aerosol
903 on southerly flow days and associated changes in cloud microphysical properties are important findings with
904 implications for weather, health, coastal ecology, and aviation.
905

906 Data availability

907 Airborne data used in this work can be accessed at <https://doi.org/10.6084/m9.figshare.5099983.v11> (Sorooshian et
908 al., 2017). ~~Buoy~~ Buoy data from the NOAA's NDBC can be accessed at <https://www.ndbc.noaa.gov/>. The archived
909 data from GOES-West Full Disk Cloud Product (GOES-15) can be accessed at <https://satcorps.larc.nasa.gov/>. The
910 archived surface weather plots from NOAA's WPC can be accessed at
911 https://www.wpc.ncep.noaa.gov/archives/web_pages/sfc/sfc_archive.php. The surface data from IMPROVE can be
912 accessed at <http://views.cira.colostate.edu/fed/>. The MODIS-Aqua data can be accessed through NASA Giovanni at
913 <https://giovanni.gsfc.nasa.gov/giovanni/>. The FIRMS data can be accessed at <https://earthdata.nasa.gov/firms>.

914 Author contributions

915 AW and PX aided with access and interpretation of COAMPS and NAAPS data, respectively. KZ and GB conducted
916 the data analysis. KZ and AS conducted data interpretation. KZ and AS prepared the manuscript. All authors edited
917 the manuscript.

918 **Competing interests**

919 At least one of the (co-)authors is a member of the editorial board of Atmospheric Chemistry and Physics.

920 **Disclaimer**

921 Publisher's note: Copernicus Publications remains neutral with regard to jurisdictional claims in published maps and
922 institutional affiliations.

923

924 **Acknowledgements**

925 The authors acknowledge NPS staff for successfully conducting Twin Otter flights and all others who were involved
926 in the airborne campaigns. We thank Ewan Crosbie for useful discussions about this work.

927 **Financial support**

928 This work was funded by Office of Naval Research grant N00014-21-1-2115.

929

930

931 **References**

932

933 AzadiAghdam, M., Braun, R. A., Edwards, E. L., Bañaga, P. A., Cruz, M. T., Betito, G., Cambaliza, M. O.,
934 Dadashazar, H., Lorenzo, G. R., Ma, L., MacDonald, A. B., Nguyen, P., Simpas, J. B., Stahl, C., and Sorooshian, A.:
935 On the nature of sea salt aerosol at a coastal megacity: Insights from Manila, Philippines in Southeast Asia,
936 Atmospheric Environment, 216, 116922, <https://doi.org/10.1016/j.atmosenv.2019.116922>, 2019.
937 Blanchard, D. C. and Woodcock, A. H.: Bubble Formation and Modification in the Sea and its Meteorological
938 Significance, Tellus, 9, 145–158, [10.3402/tellusa.v9i2.9094](https://doi.org/10.3402/tellusa.v9i2.9094), 1957.
939 Bond, N. A., Mass, C. F., and Overland, J. E.: Coastally Trapped Wind Reversals along the United States West
940 Coast during the Warm Season. Part I: Climatology and Temporal Evolution, Monthly Weather Review, 124, 430–
941 445, [https://doi.org/10.1175/1520-0493\(1996\)124<0430:CTWRAT>2.0.CO;2](https://doi.org/10.1175/1520-0493(1996)124<0430:CTWRAT>2.0.CO;2), 1996.
942 Braun, R. A., Dadashazar, H., MacDonald, A. B., Aldhaif, A. M., Maudlin, L. C., Crosbie, E., Aghdam, M. A.,
943 Hossein Mardi, A., and Sorooshian, A.: Impact of Wildfire Emissions on Chloride and Bromide Depletion in Marine
944 Aerosol Particles, Environmental Science & Technology, 51, 9013–9021, [10.1021/acs.est.7b02039](https://doi.org/10.1021/acs.est.7b02039), 2017.
945 Cahill, T. A., Ashbaugh, L. L., Eldred, R. A., Feeney, P. J., Kusko, B. H., and Floechini, R. G.: Comparisons
946 Between Size Segregated Resuspended Soil Samples and Ambient Aerosols in the Western United States, in:
947 Atmospheric Aerosol, ACS Symposium Series, 167, AMERICAN CHEMICAL SOCIETY, 269–285,
948 [doi:10.1021/bk-1981-0167.ch015](https://doi.org/10.1021/bk-1981-0167.ch015)
949 [10.1021/bk-1981-0167.ch015](https://doi.org/10.1021/bk-1981-0167.ch015), 1981.
950 Celso, V., Dabek-Zlotorzynska, E., and McCurdy, M.: Chemical Characterization of Exhaust Emissions from
951 Selected Canadian Marine Vessels: The Case of Trace Metals and Lanthanoids, Environmental Science &
952 Technology, 49, 5220–5226, [10.1021/acs.est.5b00127](https://doi.org/10.1021/acs.est.5b00127), 2015.
953 Chow, J. C., Watson, J. G., Pritchett, L. C., Pierson, W. R., Frazier, C. A., and Purcell, R. G.: The dri thermal/optical
954 reflectance carbon analysis system: description, evaluation and applications in U.S. Air quality studies, Atmospheric
955 Environment. Part A. General Topics, 27, 1185–1201, [https://doi.org/10.1016/0960-1686\(93\)90245-T](https://doi.org/10.1016/0960-1686(93)90245-T), 1993.
956 Coggon, M. M., Sorooshian, A., Wang, Z., Craven, J. S., Metcalf, A. R., Lin, J. J., Nenes, A., Jonsson, H. H.,
957 Flagan, R. C., and Seinfeld, J. H.: Observations of continental biogenic impacts on marine aerosol and clouds off the
958 coast of California, Journal of Geophysical Research: Atmospheres, 119, 6724–6748, [10.1002/2013jd021228](https://doi.org/10.1002/2013jd021228), 2014.
959 Coggon, M. M., Sorooshian, A., Wang, Z., Metcalf, A. R., Frossard, A. A., Lin, J. J., Craven, J. S., Nenes, A.,
960 Jonsson, H. H., Russell, L. M., Flagan, R. C., and Seinfeld, J. H.: Ship impacts on the marine atmosphere: insights
961 into the contribution of shipping emissions to the properties of marine aerosol and clouds, Atmospheric Chemistry
962 and Physics, 12, 8439–8458, [10.5194/acp-12-8439-2012](https://doi.org/10.5194/acp-12-8439-2012), 2012.

963 Corbett, J. J. and Fischbeck, P.: Emissions from Ships, *Science*, 278, 823–824, doi:10.1126/science.278.5339.823,
964 1997.

965 Corbin, J. C., Mensah, A. A., Pieber, S. M., Orasche, J., Michalke, B., Zanatta, M., Czech, H., Massabò, D., Buatier
966 de Mongeot, F., Mennucci, C., El Haddad, I., Kumar, N. K., Stengel, B., Huang, Y., Zimmermann, R., Prévôt, A. S.
967 H., and Gysel, M.: Trace Metals in Soot and PM_{2.5} from Heavy Fuel Oil Combustion in a Marine Engine,
968 *Environmental Science & Technology*, 52, 6714–6722, 10.1021/acs.est.8b01764, 2018.

969 Council, N. R.: *Coastal Meteorology: A Review of the State of the Science*, Washington, D.C., 99,
970 <https://doi.org/10.17226/1991>, 1992.

971 Crosbie, E., Wang, Z., Sorooshian, A., Chuang, P. Y., Craven, J. S., Coggon, M. M., Brunke, M., Zeng, X., Jonsson,
972 H., Woods, R. K., Flagan, R. C., and Seinfeld, J. H.: Stratocumulus Cloud Clearings and Notable Thermodynamic
973 and Aerosol Contrasts across the Clear–Cloudy Interface, *Journal of the Atmospheric Sciences*, 73, 1083–1099,
974 <https://doi.org/10.1175/JAS-D-15-0137.1>, 2016.

975 Dadashazar, H., Ma, L., and Sorooshian, A.: Sources of pollution and interrelationships between aerosol and
976 precipitation chemistry at a central California site, *Science of The Total Environment*, 651, 1776–1787,
977 <https://doi.org/10.1016/j.scitotenv.2018.10.086>, 2019.

978 Dadashazar, H., Crosbie, E., Majidi, M. S., Panahi, M., Moghaddam, M. A., Behrangi, A., Brunke, M., Zeng, X.,
979 Jonsson, H. H., and Sorooshian, A.: Stratocumulus cloud clearings: statistics from satellites, reanalysis models, and
980 airborne measurements, *Atmospheric Chemistry and Physics*, 20, 4637–4665, 10.5194/acp-20-4637-2020, 2020.

981 Dorman, C. E.: Evidence of Kelvin Waves in California's Marine Layer and Related Eddy Generation, *Monthly
982 Weather Review*, 113, 827–839, [https://doi.org/10.1175/1520-0493\(1985\)113<0827:EOKWIC>2.0.CO;2](https://doi.org/10.1175/1520-0493(1985)113<0827:EOKWIC>2.0.CO;2), 1985.

983 Edwards, E. L., Choi, Y., Crosbie, E. C., DiGangi, J. P., Diskin, G. S., Robinson, C. E., Shook, M. A., Winstead, E.
984 L., Ziemba, L. D., and Sorooshian, A.: Sea salt reactivity over the northwest Atlantic: An in-depth look using the
985 airborne ACTIVATE dataset, *EGU sphere*, 2023, 1–56, 10.5194/egusphere-2023-2575, 2023.

986 Ervens, B.: Modeling the Processing of Aerosol and Trace Gases in Clouds and Fogs, *Chemical Reviews*, 115,
987 4157–4198, 10.1021/er5005887, 2015.

988 Ervens, B., Turpin, B. J., and Weber, R. J.: Secondary organic aerosol formation in cloud droplets and aqueous
989 particles (aqSOA): a review of laboratory, field and model studies, *Atmos. Chem. Phys.*, 11, 11069–11102,
990 10.5194/acp-11-11069-2011, 2011.

991 Fitzgerald, J. W.: Marine aerosols: A review, *Atmospheric Environment. Part A. General Topics*, 25, 533–545,
992 [https://doi.org/10.1016/0960-1686\(91\)90050-H](https://doi.org/10.1016/0960-1686(91)90050-H), 1991.

993 Garreaud, R. and Rutllant, J.: Coastal Lows along the Subtropical West Coast of South America: Numerical
994 Simulation of a Typical Case, *Monthly Weather Review*, 131, 891–908, [https://doi.org/10.1175/1520-0493\(2003\)131<0891:CLATSW>2.0.CO;2](https://doi.org/10.1175/1520-0493(2003)131<0891:CLATSW>2.0.CO;2), 2003.

995 Garreaud, R., Rutllant, J., and Fuenzalida, H.: Coastal Lows along the Subtropical West Coast of South America:
996 Mean Structure and Evolution, *Monthly Weather Review*, 130, 75–88, [https://doi.org/10.1175/1520-0493\(2002\)130<0075:CLATSW>2.0.CO;2](https://doi.org/10.1175/1520-0493(2002)130<0075:CLATSW>2.0.CO;2), 2002.

999 Giglio, L., Schroeder, W., Hall, J. V., and Justice, C. O.: Modis collection 6 active fire product user's guide revision
1000 A, Department of Geographical Sciences, University of Maryland, 9, 2015.

1001 Gill, A. E.: Coastally trapped waves in the atmosphere, *Quarterly Journal of the Royal Meteorological Society*, 103,
1002 431–440, <https://doi.org/10.1002/qj.49710343704>, 1977.

1003 Gonzalez, M. E., Corral, A. F., Crosbie, E., Dadashazar, H., Diskin, G. S., Edwards, E. L., Kirschler, S., Moore, R.
1004 H., Robinson, C. E., Schlosser, J. S., Shook, M., Stahl, C., Thornhill, K. L., Voigt, C., Winstead, E., Ziemba, L. D.,
1005 and Sorooshian, A.: Relationships between supermicrometer particle concentrations and cloud-water sea salt and
1006 dust concentrations: analysis of MONARC and ACTIVATE data, *Environmental Science: Atmospheres*, 2, 738–752,
1007 10.1039/d2ea00049k, 2022.

1008 Guan, S., Jackson, P. L., and Reason, C. J. C.: Numerical Modeling of a Coastal Trapped Disturbance. Part I:
1009 Comparison with Observations, *Monthly Weather Review*, 126, 972–990, [https://doi.org/10.1175/1520-0493\(1998\)126<0972:NMOACT>2.0.CO;2](https://doi.org/10.1175/1520-0493(1998)126<0972:NMOACT>2.0.CO;2), 1998.

1010 Hegg, D. A., Covert, D. S., and Jonsson, H. H.: Measurements of size-resolved hygroscopicity in the California
1011 coastal zone, *Atmos. Chem. Phys.*, 8, 7193–7203, 10.5194/acp-8-7193-2008, 2008.

1012 Hilario, M. R. A., Crosbie, E., Bañaga, P. A., Betito, G., Braun, R. A., Cambaliza, M. O., Corral, A. F., Cruz, M. T.,
1013 Dibb, J. E., Lorenzo, G. R., Macdonald, A. B., Robinson, C. E., Shook, M. A., Simpas, J. B., Stahl, C., Winstead, E.,
1014 Ziemba, L. D., and Sorooshian, A.: Particulate Oxalate To Sulfate Ratio as an Aqueous Processing Marker:
1015 Similarity Across Field Campaigns and Limitations, *Geophysical Research Letters*, 48, 10.1029/2021gl096520,
1016 2021.

1018 Hodur, R. M.: The Naval Research Laboratory's Coupled Ocean/Atmosphere Mesoscale Prediction System
1019 (COAMPS), *Monthly Weather Review*, 125, 1414-1430, [https://doi.org/10.1175/1520-](https://doi.org/10.1175/1520-0493(1997)125<1414:TNRLSC>2.0.CO;2)
1020 [0493\(1997\)125<1414:TNRLSC>2.0.CO;2](https://doi.org/10.1175/1520-0493(1997)125<1414:TNRLSC>2.0.CO;2), 1997.

1021 Hogan, T., Liu, M., Ridout, J., Peng, M., Whiteomb, T., Ruston, B., Reynolds, C., Eckermann, S., Moskaitis, J.,
1022 Baker, N., McCormack, J., Viner, K., McLay, J., Flatau, M., Xu, L., Chen, C., and Chang, S.: The Navy Global
1023 Environmental Model, *Oceanography*, 27, 116-125, [10.5670/oceanog.2014.73](https://doi.org/10.5670/oceanog.2014.73), 2014.

1024 Holland, G. J. and Leslie, L. M.: Ducted coastal ridging over S.E. Australia, *Quarterly Journal of the Royal*
1025 *Meteorological Society*, 112, 731-748, <https://doi.org/10.1002/qj.49711247310>, 1986.

1026 Juliano, T. W., Lebo, Z. J., Thompson, G., and Rahn, D. A.: A New Perspective on Coastally Trapped Disturbances
1027 Using Data from the Satellite Era, *Bulletin of the American Meteorological Society*, 100, 631-651, [10.1175/bams-d-](https://doi.org/10.1175/bams-d-18-0002.1)
1028 [18-0002.1](https://doi.org/10.1175/bams-d-18-0002.1), 2019a.

1029 Juliano, T. W., Coggon, M. M., Thompson, G., Rahn, D. A., Seinfeld, J. H., Sorooshian, A., and Lebo, Z. J.: Marine
1030 Boundary Layer Clouds Associated with Coastally Trapped Disturbances: Observations and Model Simulations,
1031 *Journal of the Atmospheric Sciences*, 76, 2963-2993, [10.1175/jas-d-18-0317.1](https://doi.org/10.1175/jas-d-18-0317.1), 2019b.

1032 Keeley, J. E. and Syphard, A. D.: Large California wildfires: 2020 fires in historical context, *Fire Ecology*, 17,
1033 [10.1186/s42408-021-00110-7](https://doi.org/10.1186/s42408-021-00110-7), 2021.

1034 Lynch, P., Reid, J. S., Westphal, D. L., Zhang, J., Hogan, T. F., Hyer, E. J., Curtis, C. A., Hegg, D. A., Shi, Y.,
1035 Campbell, J. R., Rubin, J. I., Sessions, W. R., Turk, F. J., and Walker, A. L.: An 11-year global gridded aerosol
1036 optical thickness reanalysis (v1.0) for atmospheric and climate sciences, *Geoscientific Model Development*, 9, 1489-
1037 [10.5194/gmd-9-1489-2016](https://doi.org/10.5194/gmd-9-1489-2016), 2016.

1038 Ma, L., Dadashazar, H., Braun, R. A., MacDonald, A. B., Aghdam, M. A., Maudlin, L. C., and Sorooshian, A.: Size-
1039 resolved characteristics of water-soluble particulate elements in a coastal area: Source identification, influence of
1040 wildfires, and diurnal variability, *Atmospheric Environment*, 206, 72-84,
1041 <https://doi.org/10.1016/j.atmosenv.2019.02.045>, 2019.

1042 MacDonald, A. B., Dadashazar, H., Chuang, P. Y., Crosbie, E., Wang, H., Wang, Z., Jonsson, H. H., Flagan, R. C.,
1043 Seinfeld, J. H., and Sorooshian, A.: Characteristic Vertical Profiles of Cloud-Water Composition in Marine
1044 Stratocumulus Clouds and Relationships With Precipitation, *Journal of Geophysical Research: Atmospheres*, 123,
1045 [3704-3723](https://doi.org/10.1002/2017jd027900), [10.1002/2017jd027900](https://doi.org/10.1002/2017jd027900), 2018.

1046 Mahm, W. C., Sisler, J. F., Huffman, D., Eldred, R. A., and Cahill, T. A.: Spatial and seasonal trends in particle
1047 concentration and optical extinction in the United States, *Journal of Geophysical Research: Atmospheres*, 99, 1347-
1048 [1370](https://doi.org/10.1029/93JD02916), <https://doi.org/10.1029/93JD02916>, 1994.

1049 Mardi, A. H., Dadashazar, H., Painemal, D., Shingler, T., Seaman, S. T., Fenn, M. A., Hostetler, C. A., and
1050 Sorooshian, A.: Biomass Burning Over the United States East Coast and Western North Atlantic Ocean:
1051 Implications for Clouds and Air Quality, *Journal of Geophysical Research: Atmospheres*, 126,
1052 [10.1029/2021jd034916](https://doi.org/10.1029/2021jd034916), 2021.

1053 Mardi, A. H., Dadashazar, H., MacDonald, A. B., Braun, R. A., Crosbie, E., Xian, P., Thorsen, T. J., Coggon, M. M.,
1054 Fenn, M. A., Ferrare, R. A., Hair, J. W., Woods, R. K., Jonsson, H. H., Flagan, R. C., Seinfeld, J. H., and
1055 Sorooshian, A.: Biomass Burning Plumes in the Vicinity of the California Coast: Airborne Characterization of
1056 Physicochemical Properties, Heating Rates, and Spatiotemporal Features, *Journal of Geophysical Research:*
1057 *Atmospheres*, 123, [10.1029/2018jd029134](https://doi.org/10.1029/2018jd029134), 2018.

1058 Mass, C. F. and Albright, M. D.: Coastal Southerlies and Alongshore Surges of the West Coast of North America:
1059 Evidence of Mesoscale Topographically Trapped Response to Synoptic Forcing, *Monthly Weather Review*, 115,
1060 [1707-1738](https://doi.org/10.1175/1520-0493(1987)115<1707:CSAASO>2.0.CO;2), [https://doi.org/10.1175/1520-0493\(1987\)115<1707:CSAASO>2.0.CO;2](https://doi.org/10.1175/1520-0493(1987)115<1707:CSAASO>2.0.CO;2), 1987.

1061 Mass, C. F. and Steenburgh, W. J.: An Observational and Numerical Study of an Orographically Trapped Wind
1062 Reversal along the West Coast of the United States, *Monthly Weather Review*, 128, 2363-2397,
1063 [https://doi.org/10.1175/1520-0493\(2000\)128<2363:AOANSO>2.0.CO;2](https://doi.org/10.1175/1520-0493(2000)128<2363:AOANSO>2.0.CO;2), 2000.

1064 Maudlin, L. C., Wang, Z., Jonsson, H. H., and Sorooshian, A.: Impact of wildfires on size-resolved aerosol
1065 composition at a coastal California site, *Atmospheric Environment*, 119, 59-68, [10.1016/j.atmosenv.2015.08.039](https://doi.org/10.1016/j.atmosenv.2015.08.039),
1066 2015.

1067 McNeill, V. F.: Aqueous Organic Chemistry in the Atmosphere: Sources and Chemical Processing of Organic
1068 Aerosols, *Environmental Science & Technology*, 49, 1237-1244, [10.1021/es5043707](https://doi.org/10.1021/es5043707), 2015.

1069 Melton, C., Washburn, L., and Gotschalk, C.: Wind relaxations and poleward flow events in a coastal upwelling
1070 system on the central California coast, *Journal of Geophysical Research: Oceans*, 114, [10.1029/2009jc005397](https://doi.org/10.1029/2009jc005397), 2009.

1071 Monahan, E. C., Spiel, D. E., and Davidson, K. L.: A Model of Marine Aerosol Generation Via Whitecaps and
1072 Wave Disruption, in: *Oceanic Whitecaps: And Their Role in Air-Sea Exchange Processes*, edited by: Monahan, E.
1073 C., and Nioceailh, G. M., Springer-Netherlands, Dordrecht, 167-174, [10.1007/978-94-009-4668-2_16](https://doi.org/10.1007/978-94-009-4668-2_16), 1986.

1074 Moorthy, K. K. and Satheesh, S. K.: Characteristics of aerosols over a remote island, Minicoy in the Arabian Sea:
1075 Optical properties and retrieved size characteristics, *Quarterly Journal of the Royal Meteorological Society*, 126, 81-
1076 109, <https://doi.org/10.1002/qj.49712656205>, 2000.

1077 Nuss, W. A.: Synoptic Scale Structure and the Character of Coastally Trapped Wind Reversals, *Monthly Weather*
1078 *Review*, 135, 60-81, <https://doi.org/10.1175/MWR3267.1>, 2007.

1079 Nuss, W. A., Bane, J. M., Thompson, W. T., Holt, T., Dorman, C. E., Ralph, F. M., Rotunno, R., Klemp, J. B.,
1080 Skamarock, W. C., Samelson, R. M., Rogerson, A. M., Reason, C., and Jackson, P.: Coastally Trapped Wind
1081 Reversals: Progress toward Understanding, *Bulletin of the American Meteorological Society*, 81, 719-744,
1082 [https://doi.org/10.1175/1520-0477\(2000\)081<0719:CTWRPT>2.3.CO;2](https://doi.org/10.1175/1520-0477(2000)081<0719:CTWRPT>2.3.CO;2), 2000.

1083 Painemal, D. and Zuidema, P.: Assessment of MODIS cloud effective radius and optical thickness retrievals over
1084 the Southeast Pacific with VOCALS-REX in situ measurements, *Journal of Geophysical Research: Atmospheres*,
1085 116, n/a-n/a, 10.1029/2011jd016155, 2011.

1086 Parish, T. R.: Forcing of the Summertime Low-Level Jet along the California Coast, *Journal of Applied*
1087 *Meteorology*, 39, 2421-2433, [https://doi.org/10.1175/1520-0450\(2000\)039<2421:FOTSLL>2.0.CO;2](https://doi.org/10.1175/1520-0450(2000)039<2421:FOTSLL>2.0.CO;2), 2000.

1088 Pitchford, M., Floccini, R. G., Draftz, R. G., Cahill, T. A., Ashbaugh, L. L., and Eldred, R. A.: Silicon in
1089 submicron particles in the southwest, *Atmospheric Environment* (1967), 15, 321-333, [https://doi.org/10.1016/0004-6981\(81\)90035-4](https://doi.org/10.1016/0004-6981(81)90035-4), 1981.

1090 Prabhakar, G., Ervens, B., Wang, Z., Maudlin, L. C., Coggon, M. M., Jonsson, H. H., Seinfeld, J. H., and
1091 Sorooshian, A.: Sources of nitrate in stratocumulus cloud water: Airborne measurements during the 2011 E-PEACE
1092 and 2013 NiCE studies, *Atmospheric Environment*, 97, 166-173, <https://doi.org/10.1016/j.atmosenv.2014.08.019>,
1093 2014.

1094 Pye, H. O. T., Nenes, A., Alexander, B., Ault, A. P., Barth, M. C., Clegg, S. L., Collett Jr, J. L., Fahey, K. M.,
1095 Hennigan, C. J., Herrmann, H., Kanakidou, M., Kelly, J. T., Ku, I. T., McNeill, V. F., Riemer, N., Schaefer, T., Shi,
1096 G., Tilgner, A., Walker, J. T., Wang, T., Weber, R., Xing, J., Zaveri, R. A., and Zuend, A.: The acidity of
1097 atmospheric particles and clouds, *Atmos. Chem. Phys.*, 20, 4809-4888, 10.5194/acp-20-4809-2020, 2020.

1098 Rahn, D. A. and Parish, T. R.: Diagnosis of the Forcing and Structure of the Coastal Jet near Cape Mendocino Using
1099 In Situ Observations and Numerical Simulations, *Journal of Applied Meteorology and Climatology*, 46, 1455-1468,
1100 <https://doi.org/10.1175/JAM2546.1>, 2007.

1101 Rahn, D. A. and Parish, T. R.: Cessation of the 22-25 June 2006 Coastally Trapped Wind Reversal, *Journal of*
1102 *Applied Meteorology and Climatology*, 49, 1412-1428, <https://doi.org/10.1175/2010JAMC2242.1>, 2010.

1103 Ralph, F. M., Armi, L., Bane, J. M., Dorman, C., Neff, W. D., Neiman, P. J., Nuss, W., and Persson, P. O. G.:
1104 Observations and Analysis of the 10-11 June 1994 Coastally Trapped Disturbance, *Monthly Weather Review*, 126,
1105 2435-2465, [https://doi.org/10.1175/1520-0493\(1998\)126<2435:OAAOTJ>2.0.CO;2](https://doi.org/10.1175/1520-0493(1998)126<2435:OAAOTJ>2.0.CO;2), 1998.

1106 Reason, C. J. C. and Jury, M. R.: On the generation and propagation of the southern African coastal low, *Quarterly*
1107 *Journal of the Royal Meteorological Society*, 116, 1133-1151, <https://doi.org/10.1002/qj.49711649507>, 1990.

1108 Reason, C. J. C., Tory, K. J., and Jackson, P. L.: Evolution of a Southeast Australian Coastally Trapped Disturbance,
1109 *Meteorology and Atmospheric Physics*, 70, 141-165, 10.1007/s007030050031, 1999.

1110 Reid, H. J. and Leslie, L. M.: Modeling Coastally Trapped Wind Surges over Southeastern Australia. Part I: Timing
1111 and Speed of Propagation, *Weather and Forecasting*, 14, 53-66, [https://doi.org/10.1175/1520-0434\(1999\)014<0053:MCTWSO>2.0.CO;2](https://doi.org/10.1175/1520-0434(1999)014<0053:MCTWSO>2.0.CO;2), 1999.

1112 Rogerson, A. M. and Samelson, R. M.: Synoptic Forcing Of Coastal Trapped Disturbances in the Marine
1113 Atmospheric Boundary Layer, *Journal of Atmospheric Sciences*, 52, 2025-2040, [https://doi.org/10.1175/1520-0469\(1995\)052<2025:SFOCTD>2.0.CO;2](https://doi.org/10.1175/1520-0469(1995)052<2025:SFOCTD>2.0.CO;2), 1995.

1114 Rolph, G., Stein, A., and Stunder, B.: Real-time Environmental Applications and Display sYstem: READY,
1115 *Environmental Modelling & Software*, 95, 210-228, <https://doi.org/10.1016/j.envsoft.2017.06.025>, 2017.

1116 Russell, L. M., Sorooshian, A., Seinfeld, J. H., Albrecht, B. A., Nenes, A., Ahlm, L., Chen, Y. C., Coggon, M.,
1117 Craven, J. S., Flagan, R. C., Frossard, A. A., Jonsson, H., Jung, E., Lin, J. J., Metcalf, A. R., Modini, R.,
1118 Mülmenstädt, J., Roberts, G., Shingler, T., Song, S., Wang, Z., and Wonaschütz, A.: Eastern Pacific Emitted
1119 Aerosol Cloud Experiment, *Bulletin of the American Meteorological Society*, 94, 709-729, 10.1175/bams-d-12-00015.1, 2013.

1120 Schlosser, J. S., Braun, R. A., Bradley, T., Dadashazar, H., Macdonald, A. B., Aldhaif, A. A., Aghdam, M. A.,
1121 Mardi, A. H., Xian, P., and Sorooshian, A.: Analysis of aerosol composition data for western United States wildfires
1122 between 2005 and 2015: Dust emissions, chloride depletion, and most enhanced aerosol constituents, *Journal of*
1123 *Geophysical Research: Atmospheres*, 122, 8951-8966, 10.1002/2017jd026547, 2017.

1128 Skamarock, W. C., Rotunno, R., and Klemp, J. B.: Models of Coastally Trapped Disturbances, *Journal of the*
1129 *Atmospheric Sciences*, 56, 3349–3365, [https://doi.org/10.1175/1520-0469\(1999\)056<3349:MOCTD>2.0.CO;2](https://doi.org/10.1175/1520-0469(1999)056<3349:MOCTD>2.0.CO;2),
1130 1999.

1131 Sorooshian, A., Wang, Z., Coggon, M. M., Jonsson, H. H., and Ervens, B.: Observations of Sharp Oxalate
1132 Reductions in Stratocumulus Clouds at Variable Altitudes: Organic Acid and Metal Measurements During the 2011
1133 E-PEACE Campaign, *Environmental Science & Technology*, 47, 7747–7756, [10.1021/es4012383](https://doi.org/10.1021/es4012383), 2013.

1134 Sorooshian, A., Macdonald, A. B., Dadashazar, H., Bates, K. H., Coggon, M. M., Craven, J. S., Crosbie, E., Hersey,
1135 S. P., Hodas, N., Lin, J. J., Negrón Marty, A., Maudlin, L. C., Metcalf, A. R., Murphy, S. M., Padró, L. T.,
1136 Prabhakar, G., Rissman, T. A., Shingler, T., Varutbangkul, V., Wang, Z., Woods, R. K., Chuang, P. Y., Nenes, A.,
1137 Jonsson, H. H., Flagan, R. C., and Seinfeld, J. H.: A multi-year data set on aerosol-cloud-precipitation-meteorology
1138 interactions for marine stratocumulus clouds, *Scientific Data*, 5, 180026, [10.1038/sdata.2018.26](https://doi.org/10.1038/sdata.2018.26), 2018.

1139 Sorooshian, A., Anderson, B., Bauer, S. E., Braun, R. A., Cairns, B., Crosbie, E., Dadashazar, H., Diskin, G.,
1140 Ferrare, R., Flagan, R. C., Hair, J., Hostetler, C., Jonsson, H. H., Kleb, M. M., Liu, H., Macdonald, A. B.,
1141 McComiskey, A., Moore, R., Painemal, D., Russell, L. M., Seinfeld, J. H., Shook, M., Smith, W. L., Thornhill, K.,
1142 Tselioudis, G., Wang, H., Zeng, X., Zhang, B., Ziemba, L., and Zuidema, P.: Aerosol-Cloud-Meteorology
1143 Interaction Airborne Field Investigations: Using Lessons Learned from the U.S. West Coast in the Design of
1144 ACTIVATE off the U.S. East Coast, *Bulletin of the American Meteorological Society*, 100, 1511–1528,
1145 [10.1175/bams-d-18-0100.1](https://doi.org/10.1175/bams-d-18-0100.1), 2019.

1146 Sorooshian, A., MacDonald, A. B., Dadashazar, H., Bates, K. H., Coggon, M. M., Craven, J. S., Crosbie, E.,
1147 Edwards, E. L., Hersey, S. P., Hodas, N., Lin, J. J., Mardi, A. H., Negrón Marty, A., Maudlin, L. C., Metcalf, A. R.,
1148 Murphy, S. M., Padró, L. T., Prabhakar, G., Rissman, T. A., Schlosser, J. S., Shingler, T., Varutbangkul, V., Wang,
1149 Z., Woods, R. K., Chuang, P. Y., Nenes, A., Jonsson, H. H., Flagan, R. C., Seinfeld, J. H., and Stahl, C.: A Multi-
1150 Year Data Set on Aerosol-Cloud-Precipitation Meteorology Interactions for Marine Stratocumulus Clouds, *figshare*,
1151 <https://doi.org/10.6084/m9.figshare.5099983.v11>, 2017.

1152 Stahl, C., Cruz, M. T., Bañaga, P. A., Betito, G., Braun, R. A., Aghdam, M. A., Cambaliza, M. O., Lorenzo, G. R.,
1153 MacDonald, A. B., Hilario, M. R. A., Pabroa, P. C., Yee, J. R., Simpas, J. B., and Sorooshian, A.: Sources and
1154 characteristics of size-resolved particulate organic acids and methanesulfonate in a coastal megacity: Manila,
1155 Philippines, *Atmos. Chem. Phys.*, 20, 15907–15935, [10.5194/acp-20-15907-2020](https://doi.org/10.5194/acp-20-15907-2020), 2020.

1156 Stein, A. F., Draxler, R. R., Rolph, G. D., Stunder, B. J. B., Cohen, M. D., and Ngan, F.: NOAA's HYSPLIT
1157 Atmospheric Transport and Dispersion Modeling System, *Bulletin of the American Meteorological Society*, 96,
1158 2059–2077, <https://doi.org/10.1175/BAMS-D-14-00110.1>, 2015.

1159 Thompson, W. T., Burk, S. D., and Lewis, J.: Fog and low clouds in a coastally-trapped disturbance, *Journal of*
1160 *Geophysical Research: Atmospheres*, 110, [10.1029/2004jd005522](https://doi.org/10.1029/2004jd005522), 2005.

1161 Twomey, S.: Pollution and the planetary albedo, *Atmospheric Environment* (1967), 8, 1251–1256,
1162 [https://doi.org/10.1016/0004-6981\(74\)90004-3](https://doi.org/10.1016/0004-6981(74)90004-3), 1974.

1163 Wang, Z., Sorooshian, A., Prabhakar, G., Coggon, M. M., and Jonsson, H. H.: Impact of emissions from shipping,
1164 land, and the ocean on stratocumulus cloud water elemental composition during the 2011 E-PEACE field campaign,
1165 *Atmospheric Environment*, 89, 570–580, <https://doi.org/10.1016/j.atmosenv.2014.01.020>, 2014.

1166 Wang, Z., Mora Ramirez, M., Dadashazar, H., Macdonald, A. B., Crosbie, E., Bates, K. H., Coggon, M. M., Craven,
1167 J. S., Lynch, P., Campbell, J. R., Azadi Aghdam, M., Woods, R. K., Jonsson, H., Flagan, R. C., Seinfeld, J. H., and
1168 Sorooshian, A.: Contrasting cloud composition between coupled and decoupled marine boundary layer clouds,
1169 *Journal of Geophysical Research: Atmospheres*, 121, 611–619, [10.1002/2016jd025695](https://doi.org/10.1002/2016jd025695), 2016.

1170 Watson, J. G., Chow, J. C., Lowenthal, D. H., Pritchett, L. C., Frazier, C. A., Neuroth, G. R., and Robbins, R.:
1171 Differences in the carbon composition of source profiles for diesel- and gasoline-powered vehicles, *Atmospheric*
1172 *Environment*, 28, 2493–2505, [https://doi.org/10.1016/1352-2310\(94\)90400-6](https://doi.org/10.1016/1352-2310(94)90400-6), 1994.

1173 Winant, C. D., Beardsley, R. C., and Davis, R. E.: Moored wind, temperature, and current observations made during
1174 Coastal Ocean Dynamics Experiments 1 and 2 over the Northern California Continental Shelf and upper slope,
1175 *Journal of Geophysical Research: Oceans*, 92, 1569–1604, <https://doi.org/10.1029/JC092iC02p01569>, 1987.

1176 Wood, R.: Stratocumulus Clouds, *Monthly Weather Review*, 140, 2373–2423, [10.1175/mwr-d-11-00121.1](https://doi.org/10.1175/mwr-d-11-00121.1), 2012.

1177 Wu, J.: Bubble flux and marine aerosol spectra under various wind velocities, *Journal of Geophysical Research:*
1178 *Oceans*, 97, 2327–2333, <https://doi.org/10.1029/91JC02568>, 1992.

1179 AzadiAghdam, M., Braun, R. A., Edwards, E. L., Bañaga, P. A., Cruz, M. T., Betito, G., Cambaliza, M. O.,
1180 Dadashazar, H., Lorenzo, G. R., Ma, L., MacDonald, A. B., Nguyen, P., Simpas, J. B., Stahl, C., and
1181 Sorooshian, A.: On the nature of sea salt aerosol at a coastal megacity: Insights from Manila, Philippines in
1182 Southeast Asia, *Atmospheric Environment*, 216, 116922, <https://doi.org/10.1016/j.atmosenv.2019.116922>, 2019.

1183 [Blanchard, D. C. and Woodcock, A. H.: Bubble formation and modification in the sea and its meteorological](#)
1184 [significance. *Tellus*, 9, 145-158, 10.3402/tellusa.v9i2.9094, 1957.](#)

1185 [Bond, N. A., Mass, C. F., and Overland, J. E.: Coastally trapped wind reversals along the United States west coast](#)
1186 [during the warm season. Part I: Climatology and temporal evolution. *Monthly Weather Review*, 124, 430-445,](#)
1187 [https://doi.org/10.1175/1520-0493\(1996\)124<0430:CTWRAT>2.0.CO;2](https://doi.org/10.1175/1520-0493(1996)124<0430:CTWRAT>2.0.CO;2), 1996.

1188 [Braun, R. A., Dadashazar, H., MacDonald, A. B., Aldhaif, A. M., Maudlin, L. C., Crosbie, E., Aghdam, M. A.,](#)
1189 [Hossein Mardi, A., and Sorooshian, A.: Impact of wildfire emissions on chloride and bromide depletion in](#)
1190 [marine aerosol particles. *Environmental Science & Technology*, 51, 9013-9021,](#)
1191 <https://doi.org/10.1021/acs.est.7b02039>, 2017.

1192 [Cahill, T. A., Ashbaugh, L. L., Eldred, R. A., Feeny, P. J., Kusko, B. H., and Flocchini, R. G.: Comparisons between](#)
1193 [size-segregated resuspended soil samples and ambient aerosols in the western United States. in: *Atmospheric*](#)
1194 [Aerosol. ACS Symposium Series, 167, American Chemical Society, 269-285, https://doi.org/10.1021/bk-1981-](#)
1195 [0167.ch015, 1981.](#)

1196 [Celo, V., Dabek-Zlotorzynska, E., and McCurdy, M.: Chemical characterization of exhaust emissions from selected](#)
1197 [Canadian marine vessels: The case of trace metals and lanthanoids. *Environmental Science & Technology*, 49,](#)
1198 [5220-5226, https://doi.org/10.1021/acs.est.5b00127, 2015.](#)

1199 [Chow, J. C., Watson, J. G., Pritchett, L. C., Pierson, W. R., Frazier, C. A., and Purcell, R. G.: The dri thermal/optical](#)
1200 [reflectance carbon analysis system: description, evaluation and applications in U.S. Air quality studies,](#)
1201 [Atmospheric Environment. Part A. General Topics, 27, 1185-1201, https://doi.org/10.1016/0960-](#)
1202 [1686\(93\)90245-T, 1993.](#)

1203 [Coggon, M. M., Sorooshian, A., Wang, Z., Metcalf, A. R., Frossard, A. A., Lin, J. J., Craven, J. S., Nenes, A.,](#)
1204 [Jonsson, H. H., Russell, L. M., Flagan, R. C., and Seinfeld, J. H.: Ship impacts on the marine atmosphere:](#)
1205 [insights into the contribution of shipping emissions to the properties of marine aerosol and clouds, *Atmospheric*](#)
1206 [Chemistry and Physics, 12, 8439-8458, https://doi.org/10.5194/acp-12-8439-2012, 2012.](#)

1207 [Coggon, M. M., Sorooshian, A., Wang, Z., Craven, J. S., Metcalf, A. R., Lin, J. J., Nenes, A., Jonsson, H. H., Flagan,](#)
1208 [R. C., and Seinfeld, J. H.: Observations of continental biogenic impacts on marine aerosol and clouds off the](#)
1209 [coast of California. *Journal of Geophysical Research: Atmospheres*, 119, 6724-6748,](#)
1210 <https://doi.org/10.1002/2013jd021228>, 2014.

1211 [Corbett, J. J. and Fischbeck, P.: Emissions from ships, *Science*, 278, 823-824,](#)
1212 <https://doi.org/10.1126/science.278.5339.823>, 1997.

1213 [Corbin, J. C., Mensah, A. A., Pieber, S. M., Orasche, J., Michalke, B., Zanatta, M., Czech, H., Massabò, D., Buatier](#)
1214 [de Mongeot, F., Mennucci, C., El Haddad, I., Kumar, N. K., Stengel, B., Huang, Y., Zimmermann, R., Prévôt, A.](#)
1215 [S. H., and Gysel, M.: Trace metals in soot and PM_{2.5} from heavy-fuel-oil combustion in a marine engine,](#)
1216 [Environmental Science & Technology, 52, 6714-6722, https://doi.org/10.1021/acs.est.8b01764, 2018.](#)

1217 [Crosbie, E., Wang, Z., Sorooshian, A., Chuang, P. Y., Craven, J. S., Coggon, M. M., Brunke, M., Zeng, X., Jonsson,](#)
1218 [H., Woods, R. K., Flagan, R. C., and Seinfeld, J. H.: Stratocumulus cloud clearings and notable thermodynamic](#)
1219 [and aerosol contrasts across the clear–cloudy interface. *Journal of the Atmospheric Sciences*, 73, 1083-1099,](#)
1220 <https://doi.org/10.1175/JAS-D-15-0137.1>, 2016.

1221 [Dadashazar, H., Ma, L., and Sorooshian, A.: Sources of pollution and interrelationships between aerosol and](#)
1222 [precipitation chemistry at a central California site. *Science of The Total Environment*, 651, 1776-1787,](#)
1223 <https://doi.org/10.1016/j.scitotenv.2018.10.086>, 2019.

1224 [Dadashazar, H., Crosbie, E., Majidi, M. S., Panahi, M., Moghaddam, M. A., Behrangi, A., Brunke, M., Zeng, X.,](#)
1225 [Jonsson, H. H., and Sorooshian, A.: Stratocumulus cloud clearings: statistics from satellites, reanalysis models,](#)

1226 [and airborne measurements, Atmospheric Chemistry and Physics, 20, 4637-4665, https://doi.org/10.5194/acp-](https://doi.org/10.5194/acp-20-4637-2020)
1227 [20-4637-2020, 2020.](https://doi.org/10.5194/acp-20-4637-2020)

1228 Dorman, C. E.: Evidence of Kelvin waves in California's marine layer and related eddy generation, *Monthly*
1229 *Weather Review*, 113, 827-839, [https://doi.org/10.1175/1520-0493\(1985\)113<0827:EOKWIC>2.0.CO;2](https://doi.org/10.1175/1520-0493(1985)113<0827:EOKWIC>2.0.CO;2), 1985.

1230 Edwards, E. L., Choi, Y., Crosbie, E. C., DiGangi, J. P., Diskin, G. S., Robinson, C. E., Shook, M. A., Winstead, E.
1231 L., Ziemba, L. D., and Sorooshian, A.: Sea salt reactivity over the northwest Atlantic: An in-depth look using
1232 the airborne ACTIVATE dataset, *EGUosphere*, 2023, 1-56, <https://doi.org/10.5194/egusphere-2023-2575>, 2023.

1233 Ervens, B., Turpin, B. J., and Weber, R. J.: Secondary organic aerosol formation in cloud droplets and aqueous
1234 particles (aqSOA): a review of laboratory, field and model studies, *Atmospheric Chemistry and Physics*, 11,
1235 11069-11102, <https://doi.org/10.5194/acp-11-11069-2011>, 2011.

1236 Ervens, B.: Modeling the processing of aerosol and trace gases in clouds and fogs, *Chemical Reviews*, 115, 4157-
1237 4198, <https://doi.org/10.1021/cr5005887>, 2015.

1238 Fitzgerald, J. W.: Marine aerosols: A review, *Atmospheric Environment. Part A. General Topics*, 25, 533-545,
1239 [https://doi.org/10.1016/0960-1686\(91\)90050-H](https://doi.org/10.1016/0960-1686(91)90050-H), 1991.

1240 Garreaud, R., Rutllant, J., and Fuenzalida, H.: Coastal lows along the subtropical west coast of South America:
1241 Mean structure and evolution, *Monthly Weather Review*, 130, 75-88, [https://doi.org/10.1175/1520-](https://doi.org/10.1175/1520-0493(2002)130<0075:CLATSW>2.0.CO;2)
1242 [0493\(2002\)130<0075:CLATSW>2.0.CO;2](https://doi.org/10.1175/1520-0493(2002)130<0075:CLATSW>2.0.CO;2), 2002.

1243 Garreaud, R. and Rutllant, J.: Coastal lows along the subtropical west coast of South America: Numerical simulation
1244 of a typical case, *Monthly Weather Review*, 131, 891-908, [https://doi.org/10.1175/1520-](https://doi.org/10.1175/1520-0493(2003)131<0891:CLATSW>2.0.CO;2)
1245 [0493\(2003\)131<0891:CLATSW>2.0.CO;2](https://doi.org/10.1175/1520-0493(2003)131<0891:CLATSW>2.0.CO;2), 2003.

1246 Giglio, L., Schroeder, W., Hall, J. V., and Justice, C. O.: Modis collection 6 active fire product user's guide revision
1247 A, Department of Geographical Sciences. University of Maryland, 9, 2015.

1248 Gill, A. E.: Coastally trapped waves in the atmosphere, *Quarterly Journal of the Royal Meteorological Society*, 103,
1249 431-440, <https://doi.org/10.1002/qj.49710343704>, 1977.

1250 Gonzalez, M. E., Corral, A. F., Crosbie, E., Dadashazar, H., Diskin, G. S., Edwards, E.-L., Kirschler, S., Moore, R.
1251 H., Robinson, C. E., Schlosser, J. S., Shook, M., Stahl, C., Thornhill, K. L., Voigt, C., Winstead, E., Ziemba, L.
1252 D., and Sorooshian, A.: Relationships between supermicrometer particle concentrations and cloud water sea salt
1253 and dust concentrations: analysis of MONARC and ACTIVATE data, *Environmental Science: Atmospheres*, 2,
1254 738-752, <https://doi.org/10.1039/d2ea00049k>, 2022.

1255 Guan, S., Jackson, P. L., and Reason, C. J. C.: Numerical modeling of a coastal trapped disturbance. Part I:
1256 Comparison with observations, *Monthly Weather Review*, 126, 972-990, [https://doi.org/10.1175/1520-](https://doi.org/10.1175/1520-0493(1998)126<0972:NMOACT>2.0.CO;2)
1257 [0493\(1998\)126<0972:NMOACT>2.0.CO;2](https://doi.org/10.1175/1520-0493(1998)126<0972:NMOACT>2.0.CO;2), 1998.

1258 Hegg, D. A., Covert, D. S., and Jonsson, H. H.: Measurements of size-resolved hygroscopicity in the California
1259 coastal zone, *Atmospheric Chemistry and Physics*, 8, 7193-7203, <https://doi.org/10.5194/acp-8-7193-2008>,
1260 2008.

1261 Hilario, M. R. A., Crosbie, E., Bañaga, P. A., Betito, G., Braun, R. A., Cambaliza, M. O., Corral, A. F., Cruz, M. T.,
1262 Dibb, J. E., Lorenzo, G. R., MacDonald, A. B., Robinson, C. E., Shook, M. A., Simpas, J. B., Stahl, C.,
1263 Winstead, E., Ziemba, L. D., and Sorooshian, A.: Particulate oxalate-to-sulfate ratio as an aqueous processing
1264 marker: Similarity across field campaigns and limitations, *Geophysical Research Letters*, 48,
1265 <https://doi.org/10.1029/2021gl096520>, 2021.

1266 Hodur, R. M.: The Naval Research Laboratory's Coupled Ocean/Atmosphere Mesoscale Prediction System
1267 (COAMPS), *Monthly Weather Review*, 125, 1414-1430, [https://doi.org/10.1175/1520-](https://doi.org/10.1175/1520-0493(1997)125<1414:TNRLSC>2.0.CO;2)
1268 [0493\(1997\)125<1414:TNRLSC>2.0.CO;2](https://doi.org/10.1175/1520-0493(1997)125<1414:TNRLSC>2.0.CO;2), 1997.

1269 [Hogan, T., Liu, M., Ridout, J., Peng, M., Whitcomb, T., Ruston, B., Reynolds, C., Eckermann, S., Moskaitis, J.,](#)
 1270 [Baker, N., McCormack, J., Viner, K., McLay, J., Flatau, M., Xu, L., Chen, C., and Chang, S.: The Navy Global](#)
 1271 [Environmental Model, *Oceanography*, 27, 116-125, <https://doi.org/10.5670/oceanog.2014.73>, 2014.](#)

1272 [Holland, G. J. and Leslie, L. M.: Ducted coastal ridging over S.E. Australia, *Quarterly Journal of the Royal*](#)
 1273 [Meteorological Society, 112, 731-748, <https://doi.org/10.1002/qj.49711247310>, 1986.](#)

1274 [Juliano, T. W., Lebo, Z. J., Thompson, G., and Rahn, D. A.: A new perspective on coastally trapped disturbances](#)
 1275 [using data from the satellite era, *Bulletin of the American Meteorological Society*, 100, 631-651,](#)
 1276 [https://doi.org/10.1175/bams-d-18-0002.1, 2019a.](#)

1277 [Juliano, T. W., Coggon, M. M., Thompson, G., Rahn, D. A., Seinfeld, J. H., Sorooshian, A., and Lebo, Z. J.: Marine](#)
 1278 [boundary layer clouds associated with coastally trapped disturbances: Observations and model simulations,](#)
 1279 [Journal of the Atmospheric Sciences, 76, 2963-2993, <https://doi.org/10.1175/jas-d-18-0317.1>, 2019b.](#)

1280 [Juliano, T. W. and Lebo, Z. J.: Linking large-scale circulation patterns to low-cloud properties, *Atmospheric*](#)
 1281 [Chemistry and Physics, 20, 7125–7138, <https://doi.org/10.5194/acp-20-7125-2020>, 2020.](#)

1282 [Keeley, J. E. and Syphard, A. D.: Large California wildfires: 2020 fires in historical context, *Fire Ecology*, 17,](#)
 1283 [https://doi.org/10.1186/s42408-021-00110-7, 2021.](#)

1284 [Lynch, P., Reid, J. S., Westphal, D. L., Zhang, J., Hogan, T. F., Hyer, E. J., Curtis, C. A., Hegg, D. A., Shi, Y.,](#)
 1285 [Campbell, J. R., Rubin, J. I., Sessions, W. R., Turk, F. J., and Walker, A. L.: An 11-year global gridded aerosol](#)
 1286 [optical thickness reanalysis \(v1.0\) for atmospheric and climate sciences, *Geoscientific Model Development*, 9,](#)
 1287 [1489-1522, <https://doi.org/10.5194/gmd-9-1489-2016>, 2016.](#)

1288 [Ma, L., Dadashazar, H., Braun, R. A., MacDonald, A. B., Aghdam, M. A., Maudlin, L. C., and Sorooshian, A.: Size-](#)
 1289 [resolved characteristics of water-soluble particulate elements in a coastal area: Source identification, influence](#)
 1290 [of wildfires, and diurnal variability, *Atmospheric Environment*, 206, 72-84,](#)
 1291 [https://doi.org/10.1016/j.atmosenv.2019.02.045, 2019.](#)

1292 [MacDonald, A. B., Dadashazar, H., Chuang, P. Y., Crosbie, E., Wang, H., Wang, Z., Jonsson, H. H., Flagan, R. C.,](#)
 1293 [Seinfeld, J. H., and Sorooshian, A.: Characteristic vertical profiles of cloud water composition in marine](#)
 1294 [stratocumulus clouds and relationships with precipitation, *Journal of Geophysical Research: Atmospheres*, 123,](#)
 1295 [3704-3723, <https://doi.org/10.1002/2017jd027900>, 2018.](#)

1296 [Malm, W. C., Sisler, J. F., Huffman, D., Eldred, R. A., and Cahill, T. A.: Spatial and seasonal trends in particle](#)
 1297 [concentration and optical extinction in the United States, *Journal of Geophysical Research: Atmospheres*, 99,](#)
 1298 [1347-1370, <https://doi.org/10.1029/93JD02916>, 1994.](#)

1299 [Mardi, A. H., Dadashazar, H., MacDonald, A. B., Braun, R. A., Crosbie, E., Xian, P., Thorsen, T. J., Coggon, M. M.,](#)
 1300 [Fenn, M. A., Ferrare, R. A., Hair, J. W., Woods, R. K., Jonsson, H. H., Flagan, R. C., Seinfeld, J. H., and](#)
 1301 [Sorooshian, A.: Biomass burning plumes in the vicinity of the California coast: Airborne characterization of](#)
 1302 [physicochemical properties, heating rates, and spatiotemporal features, *Journal of Geophysical Research:*](#)
 1303 [Atmospheres, 123, <https://doi.org/10.1029/2018jd029134>, 2018.](#)

1304 [Mardi, A. H., Dadashazar, H., Painemal, D., Shingler, T., Seaman, S. T., Fenn, M. A., Hostetler, C. A., and](#)
 1305 [Sorooshian, A.: Biomass burning over the United States east coast and western North Atlantic Ocean:](#)
 1306 [Implications for clouds and air quality, *Journal of Geophysical Research: Atmospheres*, 126,](#)
 1307 [https://doi.org/10.1029/2021jd034916, 2021.](#)

1308 [Mass, C. F. and Albright, M. D.: Coastal Southerlies and Alongshore Surges of the West Coast of North America:](#)
 1309 [Evidence of mesoscale topographically trapped response to synoptic forcing, *Monthly Weather Review*, 115,](#)
 1310 [1707-1738, \[https://doi.org/10.1175/1520-0493\\(1987\\)115<1707:CSAASO>2.0.CO;2\]\(https://doi.org/10.1175/1520-0493\(1987\)115<1707:CSAASO>2.0.CO;2\), 1987.](#)

1311 [Mass, C. F. and Steenburgh, W. J.: An observational and numerical study of an orographically trapped wind reversal](#)
1312 [along the west coast of the United States, *Monthly Weather Review*, 128, 2363-2397,](#)
1313 [https://doi.org/10.1175/1520-0493\(2000\)128<2363:AOANSO>2.0.CO;2](https://doi.org/10.1175/1520-0493(2000)128<2363:AOANSO>2.0.CO;2), 2000.

1314 [Maudlin, L. C., Wang, Z., Jonsson, H. H., and Sorooshian, A.: Impact of wildfires on size-resolved aerosol](#)
1315 [composition at a coastal California site, *Atmospheric Environment*, 119, 59-68,](#)
1316 <https://doi.org/10.1016/j.atmosenv.2015.08.039>, 2015.

1317 [McNeill, V. F.: Aqueous Organic Chemistry in the Atmosphere: Sources and chemical processing of organic](#)
1318 [aerosols, *Environmental Science & Technology*, 49, 1237-1244, https://doi.org/10.1021/es5043707](#), 2015.

1319 [Melton, C., Washburn, L., and Gotschalk, C.: Wind relaxations and poleward flow events in a coastal upwelling](#)
1320 [system on the central California coast, *Journal of Geophysical Research: Oceans*, 114,](#)
1321 <https://doi.org/10.1029/2009jc005397>, 2009.

1322 [Monahan, E. C., Spiel, D. E., and Davidson, K. L.: A model of marine aerosol generation via whitecaps and wave](#)
1323 [disruption, in: *Oceanic Whitecaps: And Their Role in Air-Sea Exchange Processes*, edited by: Monahan, E. C.,](#)
1324 [and Niocaill, G. M., Springer Netherlands, Dordrecht, 167-174, https://doi.org/10.1007/978-94-009-4668-2_16,](#)
1325 [1986.](#)

1326 [Moorthy, K. K. and Satheesh, S. K.: Characteristics of aerosols over a remote island, Minicoy in the Arabian Sea:](#)
1327 [Optical properties and retrieved size characteristics, *Quarterly Journal of the Royal Meteorological Society*, 126,](#)
1328 [81-109, https://doi.org/10.1002/qj.49712656205](https://doi.org/10.1002/qj.49712656205), 2000.

1329 [National Resource Council: Coastal meteorology: A review of the state of the science, Washington, D.C., 99,](#)
1330 <https://doi.org/10.17226/1991>, 1992.

1331 [Nuss, W. A., Bane, J. M., Thompson, W. T., Holt, T., Dorman, C. E., Ralph, F. M., Rotunno, R., Klemp, J. B.,](#)
1332 [Skamarock, W. C., Samelson, R. M., Rogerson, A. M., Reason, C., and Jackson, P.: Coastally trapped wind](#)
1333 [reversals: Progress toward understanding, *Bulletin of the American Meteorological Society*, 81, 719-744,](#)
1334 [https://doi.org/10.1175/1520-0477\(2000\)081<0719:CTWRPT>2.3.CO;2](https://doi.org/10.1175/1520-0477(2000)081<0719:CTWRPT>2.3.CO;2), 2000.

1335 [Nuss, W. A.: Synoptic-scale structure and the character of coastally trapped wind reversals, *Monthly Weather*](#)
1336 [Review](#), 135, 60-81, <https://doi.org/10.1175/MWR3267.1>, 2007.

1337 [Painemal, D. and Zuidema, P.: Assessment of MODIS cloud effective radius and optical thickness retrievals over the](#)
1338 [Southeast Pacific with VOCALS-REx in situ measurements, *Journal of Geophysical Research: Atmospheres*,](#)
1339 [116, n/a-n/a, https://doi.org/10.1029/2011jd016155](https://doi.org/10.1029/2011jd016155), 2011.

1340 [Parish, T. R.: Forcing of the summertime low-level jet along the California coast, *Journal of Applied Meteorology*,](#)
1341 [39, 2421-2433, https://doi.org/10.1175/1520-0450\(2000\)039<2421:FOTSLL>2.0.CO;2](https://doi.org/10.1175/1520-0450(2000)039<2421:FOTSLL>2.0.CO;2), 2000.

1342 [Pitchford, M., Flocchini, R. G., Draftz, R. G., Cahill, T. A., Ashbaugh, L. L., and Eldred, R. A.: Silicon in submicron](#)
1343 [particles in the southwest, *Atmospheric Environment* \(1967\), 15, 321-333, https://doi.org/10.1016/0004-](#)
1344 [6981\(81\)90035-4](#), 1981.

1345 [Prabhakar, G., Ervens, B., Wang, Z., Maudlin, L. C., Coggon, M. M., Jonsson, H. H., Seinfeld, J. H., and](#)
1346 [Sorooshian, A.: Sources of nitrate in stratocumulus cloud water: Airborne measurements during the 2011 E-](#)
1347 [PEACE and 2013 NiCE studies, *Atmospheric Environment*, 97, 166-173,](#)
1348 <https://doi.org/10.1016/j.atmosenv.2014.08.019>, 2014.

1349 [Pye, H. O. T., Nenes, A., Alexander, B., Ault, A. P., Barth, M. C., Clegg, S. L., Collett Jr, J. L., Fahey, K. M.,](#)
1350 [Hennigan, C. J., Herrmann, H., Kanakidou, M., Kelly, J. T., Ku, I. T., McNeill, V. F., Riemer, N., Schaefer, T.,](#)
1351 [Shi, G., Tilgner, A., Walker, J. T., Wang, T., Weber, R., Xing, J., Zaveri, R. A., and Zuend, A.: The acidity of](#)
1352 [atmospheric particles and clouds, *Atmospheric Chemistry and Physics*, 20, 4809-4888,](#)
1353 <https://doi.org/10.5194/acp-20-4809-2020>, 2020.

1354 [Rahn, D. A. and Parish, T. R.: Diagnosis of the forcing and structure of the coastal jet near Cape Mendocino using in](#)
1355 [situ observations and numerical simulations, Journal of Applied Meteorology and Climatology, 46, 1455-1468,](#)
1356 <https://doi.org/10.1175/JAM2546.1>, 2007.

1357 [Rahn, D. A. and Parish, T. R.: Cessation of the 22–25 June 2006 coastally trapped wind reversal, Journal of Applied](#)
1358 [Meteorology and Climatology, 49, 1412-1428, https://doi.org/10.1175/2010JAMC2242.1](#), 2010.

1359 [Ralph, F. M., Armi, L., Bane, J. M., Dorman, C., Neff, W. D., Neiman, P. J., Nuss, W., and Persson, P. O. G.:](#)
1360 [Observations and analysis of the 10–11 June 1994 coastally trapped disturbance, Monthly Weather Review, 126,](#)
1361 [2435-2465, https://doi.org/10.1175/1520-0493\(1998\)126<2435:OAAOTJ>2.0.CO;2](https://doi.org/10.1175/1520-0493(1998)126<2435:OAAOTJ>2.0.CO;2), 1998.

1362 [Reason, C. J. C. and Jury, M. R.: On the generation and propagation of the southern African coastal low, Quarterly](#)
1363 [Journal of the Royal Meteorological Society, 116, 1133-1151, https://doi.org/10.1002/qj.49711649507](#), 1990.

1364 [Reason, C. J. C., Torv, K. J., and Jackson, P. L.: Evolution of a southeast Australian coastally trapped disturbance,](#)
1365 [Meteorology and Atmospheric Physics, 70, 141-165, https://doi.org/10.1007/s007030050031](#), 1999.

1366 [Reid, H. J. and Leslie, L. M.: Modeling coastally trapped wind surges over Southeastern Australia. Part I: Timing](#)
1367 [and speed of propagation, Weather and Forecasting, 14, 53-66, https://doi.org/10.1175/1520-](#)
1368 [0434\(1999\)014<0053:MCTWSO>2.0.CO;2](https://doi.org/10.1175/1520-0434(1999)014<0053:MCTWSO>2.0.CO;2), 1999.

1369 [Rogerson, A. M. and Samelson, R. M.: Synoptic forcing of coastal-trapped disturbances in the marine atmospheric](#)
1370 [boundary layer, Journal of Atmospheric Sciences, 52, 2025-2040, https://doi.org/10.1175/1520-](#)
1371 [0469\(1995\)052<2025:SFOCTD>2.0.CO;2](https://doi.org/10.1175/1520-0469(1995)052<2025:SFOCTD>2.0.CO;2), 1995.

1372 [Rolph, G., Stein, A., and Stunder, B.: Real-time Environmental Applications and Display sYstem: READY,](#)
1373 [Environmental Modelling & Software, 95, 210-228, https://doi.org/10.1016/j.envsoft.2017.06.025](#), 2017.

1374 [Russell, L. M., Sorooshian, A., Seinfeld, J. H., Albrecht, B. A., Nenes, A., Ahlm, L., Chen, Y.-C., Coggon, M.,](#)
1375 [Craven, J. S., Flagan, R. C., Frossard, A. A., Jonsson, H., Jung, E., Lin, J. J., Metcalf, A. R., Modini, R.,](#)
1376 [Mülmenstädt, J., Roberts, G., Shingler, T., Song, S., Wang, Z., and Wonaschütz, A.: Eastern Pacific Emitted](#)
1377 [Aerosol Cloud Experiment, Bulletin of the American Meteorological Society, 94, 709-729,](#)
1378 <https://doi.org/10.1175/bams-d-12-00015.1>, 2013.

1379 [Schlosser, J. S., Braun, R. A., Bradley, T., Dadashazar, H., MacDonald, A. B., Aldhaif, A. A., Aghdam, M. A., Mardi,](#)
1380 [A. H., Xian, P., and Sorooshian, A.: Analysis of aerosol composition data for western United States wildfires](#)
1381 [between 2005 and 2015: Dust emissions, chloride depletion, and most enhanced aerosol constituents, Journal of](#)
1382 [Geophysical Research: Atmospheres, 122, 8951-8966, https://doi.org/10.1002/2017jd026547](#), 2017.

1383 [Schlosser, J. S., Dadashazar, H., Edwards, E.-L., Hossein Mardi, A., Prabhakar, G., Stahl, C., Jonsson, H.H., and](#)
1384 [Sorooshian, A.: Relationships between supermicrometer sea salt aerosol and marine boundary layer conditions:](#)
1385 [Insights from repeated identical flight patterns, Journal of Geophysical Research: Atmospheres, 125,](#)
1386 [e2019JD032346, https://doi.org/10.1029/2019JD032346](https://doi.org/10.1029/2019JD032346), 2020.

1387 [Skamarock, W. C., Rotunno, R., and Klemp, J. B.: Models of coastally trapped disturbances, Journal of the](#)
1388 [Atmospheric Sciences, 56, 3349-3365, https://doi.org/10.1175/1520-0469\(1999\)056<3349:MOCTD>2.0.CO;2,](#)
1389 [1999.](#)

1390 [Sorooshian, A., Wang, Z., Coggon, M. M., Jonsson, H. H., and Ervens, B.: Observations of sharp oxalate reductions](#)
1391 [in stratocumulus clouds at variable altitudes: Organic acid and metal measurements during the 2011 E-PEACE](#)
1392 [campaign, Environmental Science & Technology, 47, 7747-7756, https://doi.org/10.1021/es4012383](#), 2013.

1393 [Sorooshian, A., MacDonald, A. B., Dadashazar, H., Bates, K. H., Coggon, M. M., Craven, J. S., Crosbie, E.,](#)
1394 [Edwards, E.-L., Hersey, S. P., Hodas, N., Lin, J. J., Mardi, A. H., Negrón Marty, A., Maudlin, L. C., Metcalf, A.](#)
1395 [R., Murphy, S. M., Padro, L. T., Prabhakar, G., Rissman, T. A., Schlosser, J. S., Shingler, T., Varutbangkul, V.,](#)
1396 [Wang, Z., Woods, R. K., Chuang, P. Y., Nenes, A., Jonsson, H. H., Flagan, R. C., Seinfeld, J. H., and Stahl, C.: A](#)

1397 [multi-year data set on aerosol-cloud-precipitation-meteorology interactions for marine stratocumulus clouds,](https://doi.org/10.6084/m9.figshare.5099983.v11)
1398 [Figshare. https://doi.org/10.6084/m9.figshare.5099983.v11, 2017.](https://doi.org/10.6084/m9.figshare.5099983.v11)

1399 [Sorooshian, A., MacDonald, A. B., Dadashazar, H., Bates, K. H., Coggon, M. M., Craven, J. S., Crosbie, E., Hersey,](#)
1400 [S. P., Hodas, N., Lin, J. J., Negrón Marty, A., Maudlin, L. C., Metcalf, A. R., Murphy, S. M., Padró, L. T.,](#)
1401 [Prabhakar, G., Rissman, T. A., Shingler, T., Varutbangkul, V., Wang, Z., Woods, R. K., Chuang, P. Y., Nenes, A.,](#)
1402 [Jonsson, H. H., Flagan, R. C., and Seinfeld, J. H.: A multi-year data set on aerosol-cloud-precipitation-](#)
1403 [meteorology interactions for marine stratocumulus clouds, *Scientific Data*, 5, 180026,](#)
1404 [https://doi.org/10.1038/sdata.2018.26, 2018.](https://doi.org/10.1038/sdata.2018.26)

1405 [Sorooshian, A., Anderson, B., Bauer, S. E., Braun, R. A., Cairns, B., Crosbie, E., Dadashazar, H., Diskin, G.,](#)
1406 [Ferrare, R., Flagan, R. C., Hair, J., Hostetler, C., Jonsson, H. H., Kleb, M. M., Liu, H., MacDonald, A. B.,](#)
1407 [McComiskey, A., Moore, R., Painemal, D., Russell, L. M., Seinfeld, J. H., Shook, M., Smith, W. L., Thornhill,](#)
1408 [K., Tselioudis, G., Wang, H., Zeng, X., Zhang, B., Ziemba, L., and Zuidema, P.: Aerosol–cloud–meteorology](#)
1409 [interaction airborne field investigations: Using lessons learned from the U.S. West Coast in the design of](#)
1410 [ACTIVATE off the U.S. east coast, *Bulletin of the American Meteorological Society*, 100, 1511-1528,](#)
1411 [https://doi.org/10.1175/bams-d-18-0100.1, 2019.](https://doi.org/10.1175/bams-d-18-0100.1)

1412 [Stahl, C., Cruz, M. T., Bañaga, P. A., Betito, G., Braun, R. A., Aghdam, M. A., Cambaliza, M. O., Lorenzo, G. R.,](#)
1413 [MacDonald, A. B., Hilario, M. R. A., Pabroa, P. C., Yee, J. R., Simpas, J. B., and Sorooshian, A.: Sources and](#)
1414 [characteristics of size-resolved particulate organic acids and methanesulfonate in a coastal megacity: Manila,](#)
1415 [Philippines, *Atmospheric Chemistry and Physics*, 20, 15907-15935, https://doi.org/10.5194/acp-20-15907-2020,](#)
1416 [2020.](#)

1417 [Stein, A. F., Draxler, R. R., Rolph, G. D., Stunder, B. J. B., Cohen, M. D., and Ngan, F.: NOAA's HYSPLIT](#)
1418 [atmospheric transport and dispersion modeling system, *Bulletin of the American Meteorological Society*, 96,](#)
1419 [2059-2077, https://doi.org/10.1175/BAMS-D-14-00110.1, 2015.](#)

1420 [Thompson, W. T., Burk, S. D., and Lewis, J.: Fog and low clouds in a coastally trapped disturbance, *Journal of*](#)
1421 [Geophysical Research: Atmospheres](#), 110, <https://doi.org/10.1029/2004jd005522>, 2005.

1422 [Twomey, S.: Pollution and the planetary albedo, *Atmospheric Environment* \(1967\), 8, 1251-1256,](#)
1423 [https://doi.org/10.1016/0004-6981\(74\)90004-3, 1974.](https://doi.org/10.1016/0004-6981(74)90004-3)

1424 [Wang, Z., Sorooshian, A., Prabhakar, G., Coggon, M. M., and Jonsson, H. H.: Impact of emissions from shipping,](#)
1425 [land, and the ocean on stratocumulus cloud water elemental composition during the 2011 E-PEACE field](#)
1426 [campaign, *Atmospheric Environment*, 89, 570-580, https://doi.org/10.1016/j.atmosenv.2014.01.020, 2014.](#)

1427 [Wang, Z., Mora Ramirez, M., Dadashazar, H., MacDonald, A. B., Crosbie, E., Bates, K. H., Coggon, M. M., Craven,](#)
1428 [J. S., Lynch, P., Campbell, J. R., Azadi Aghdam, M., Woods, R. K., Jonsson, H., Flagan, R. C., Seinfeld, J. H.,](#)
1429 [and Sorooshian, A.: Contrasting cloud composition between coupled and decoupled marine boundary layer](#)
1430 [clouds, *Journal of Geophysical Research: Atmospheres*, 121, 11,679-611,691,](#)
1431 [https://doi.org/10.1002/2016jd025695, 2016.](https://doi.org/10.1002/2016jd025695)

1432 [Watson, J. G., Chow, J. C., Lowenthal, D. H., Pritchett, L. C., Frazier, C. A., Neuroth, G. R., and Robbins, R.:](#)
1433 [Differences in the carbon composition of source profiles for diesel- and gasoline-powered vehicles,](#)
1434 [*Atmospheric Environment*, 28, 2493-2505, https://doi.org/10.1016/1352-2310\(94\)90400-6, 1994.](#)

1435 [Winant, C. D., Beardsley, R. C., and Davis, R. E.: Moored wind, temperature, and current observations made during](#)
1436 [Coastal Ocean Dynamics Experiments 1 and 2 over the Northern California Continental Shelf and upper slope,](#)
1437 [*Journal of Geophysical Research: Oceans*, 92, 1569-1604, https://doi.org/10.1029/JC092iC02p01569, 1987.](#)

1438 [Wood, R.: Stratocumulus clouds, *Monthly Weather Review*, 140, 2373-2423, https://doi.org/10.1175/mwr-d-11-](#)
1439 [00121.1, 2012.](#)

1440 Wu, J.: Bubble flux and marine aerosol spectra under various wind velocities. *Journal of Geophysical Research:*
1441 *Oceans*, 97, 2327-2333, <https://doi.org/10.1029/91JC02568>, 1992.

Formatted: Left, Indent: Left: 0", Hanging: 0.25",
Space After: 8 pt

Formatted: Font: Not Bold, Ligatures: Standard +
Contextual